Please cite this article in press as: Friedhoff et al., Stochastic reaction-diffusion modeling of calcium dynamics in 3D dendritic spines of Purkinje cells, Biophysical Journal (2021), https://doi.org/10.1016/j.bpj.2021.03.027

Biophysical *Journal*
Article

Biophysical Society

Stochastic reaction-diffusion modeling of calcium dynamics in 3D dendritic spines of Purkinje cells

Victor Nicolai Friedhoff,[1,2] Gabriela Antunes,[3] Martin Falcke,[1,2] and Fabio M. Simões de Souza[3,*]
[1]Mathematical Cell Physiology, Max Delbrück Center for Molecular Medicine, Berlin, Germany; [2]Department of Physics, Humboldt University, Berlin, Germany; and [3]Center for Mathematics, Computation, and Cognition, Federal University of ABC, São Bernardo do Campo, São Paulo, Brasil

ABSTRACT Calcium (Ca^{2+}) is a second messenger assumed to control changes in synaptic strength in the form of both long-term depression and long-term potentiation at Purkinje cell dendritic spine synapses via inositol trisphosphate (IP_3)-induced Ca^{2+} release. These Ca^{2+} transients happen in response to stimuli from parallel fibers (PFs) from granule cells and climbing fibers (CFs) from the inferior olivary nucleus. These events occur at low numbers of free Ca^{2+}, requiring stochastic single-particle methods when modeling them. We use the stochastic particle simulation program MCell to simulate Ca^{2+} transients within a three-dimensional Purkinje cell dendritic spine. The model spine includes the endoplasmic reticulum, several Ca^{2+} transporters, and endogenous buffer molecules. Our simulations successfully reproduce properties of Ca^{2+} transients in different dynamical situations. We test two different models of the IP_3 receptor (IP_3R). The model with nonlinear concentration response of binding of activating Ca^{2+} reproduces experimental results better than the model with linear response because of the filtering of noise. Our results also suggest that Ca^{2+}-dependent inhibition of the IP_3R needs to be slow to reproduce experimental results. Simulations suggest the experimentally observed optimal timing window of CF stimuli arises from the relative timing of CF influx of Ca^{2+} and IP_3 production sensitizing IP_3R for Ca^{2+}-induced Ca^{2+} release. We also model ataxia, a loss of fine motor control assumed to be the result of malfunctioning information transmission at the granule to Purkinje cell synapse, resulting in a decrease or loss of Ca^{2+} transients. Finally, we propose possible ways of recovering Ca^{2+} transients under ataxia.

SIGNIFICANCE Ca^{2+} is a second messenger that can trigger synaptic plasticity in dendritic spines of Purkinje cells, associated among other things with motor learning and motor fine control. Disrupted Ca^{2+} signals in those spines could lead to pathological conditions such as cerebelar ataxia, a lack of coordination of muscle movements. The molecular reaction mechanisms defining the spatiotemporal aspects of such Ca^{2+} signals in the noisy environment of dendritic spines in health and disease are not fully understood. Here, we develop a stochastic reaction-diffusion model in MCell to study how synaptic inputs from parallel fibers and climbing fibers reaching spines of Purkinje cells are shaping Ca^{2+} signals in healthy and pathological conditions and propose a way to recover those Ca^{2+} signals in pathological conditions.

INTRODUCTION

Ca^{2+} is a second messenger involved in many processes in eukaryotic cells. Ca^{2+} signals activate several enzymatic targets involved in the induction of synaptic plasticity in dendritic spines of Purkinje cells in the cerebellum and cause an increase or decrease of synaptic strength. Glutamate released at parallel fiber (PF) synapses binds to metabotropic glutamate receptors (mgluRs) on the Purkinje dendritic spines that activate signaling pathways associated with Ca^{2+} release from endoplasmatic reticulum intracellular stores through inositol trisphosphate receptors (IP_3Rs). This response can be further enhanced by a well-timed additional Ca^{2+} influx triggered by climbing fiber (CF) coactivation (Fig. 1; (6,7)).

Frequently, the detection and discrimination of transient Ca^{2+} signals by molecular targets in dendritic spines happen outside mass-action equilibrium, at low particle concentrations of Ca^{2+} with endogenous buffers involved, and within the rather small three-dimensional structure of the spine which entails a very noisy signaling environment. Therefore, the spatiotemporal characteristics of Ca^{2+} signals can play an important role in the induction of synaptic plasticity (8–12), determining whether long-term potentiation (LTP) or depression (LTD) occurs.

Submitted September 29, 2020, and accepted for publication March 18, 2021.

*Correspondence: fabio.souza@ufabc.edu.br

Editor: Heping Cheng.
https://doi.org/10.1016/j.bpj.2021.03.027

Please cite this article in press as: Friedhoff et al., Stochastic reaction-diffusion modeling of calcium dynamics in 3D dendritic spines of Purkinje cells, Biophysical Journal (2021), https://doi.org/10.1016/j.bpj.2021.03.027

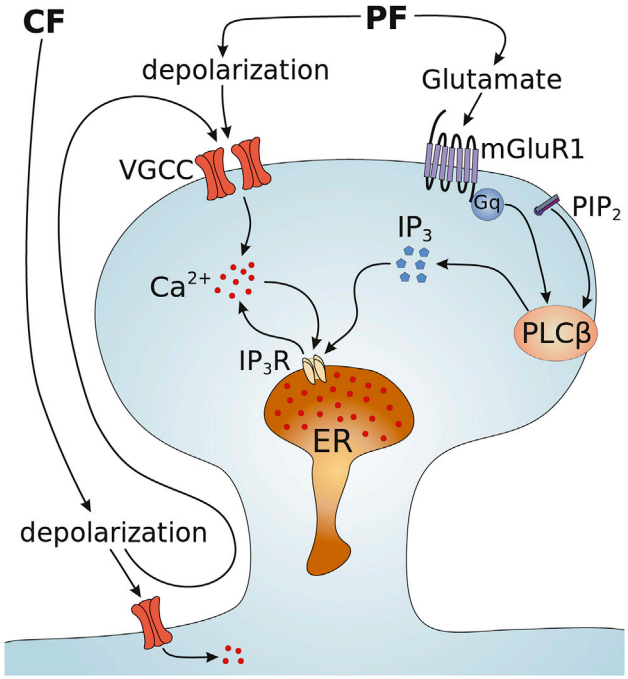

FIGURE 1 Illustration of a spine segment of a Purkinje cell showing the spine head at the top, neck in the middle, and beginning of the dendrite at the bottom. Visible are the signaling pathways of parallel and climbing fiber stimulation (1–5), which can trigger a cytosolic Ca^{2+} transient because of an opening of IP_3Rs on the ER (6,7). To see this figure in color, go online.

Computational models of the three-dimensional structure of dendritic spines and their kinetic mechanisms in their noisy environment can be very helpful in understanding the biophysical constraints shaping the Ca^{2+} dynamics that control synaptic plasticity in neurons (13). We model the system using stochastic single-particle simulations to account for the noise and low concentration properties of particles involved in the signaling processes (14–16).

Spines are dynamic extensions of neuronal dendrites and play an important role in cell signaling, neuronal excitability, information processing at the cellular level, and synaptic plasticity (17). They receive synaptic inputs from axons that release neurotransmitters, which bind to postsynaptic receptors on the spines (18,19). Because spines can react to outer and inner stimuli by changes in synaptic efficiency and in their morphological structure, their global topological arrangement becomes a mirror of sensory history and experience. Studying the dynamics of spine behavior is crucial for understanding learning, memory, motor functions, and other large-scale cognitive processes (20–24).

Spines are targets of signaling and contain molecular signaling mechanisms that regulate and are regulated by intracellular Ca^{2+} transients. Rapid Ca^{2+} release is achieved by opening of IP_3Rs, which reside on the smooth endoplasmic reticulum (ER), a Ca^{2+} store inside the spine and dendrite (6,7). IP_3Rs require inositol-1,4,5-trisphosphate (IP_3) and Ca^{2+} to open. Both IP_3 production and Ca^{2+} influx are controlled by PF and CF activity (25–28). These interacting signaling pathways give the IP_3Rs the capacity to translate fast PF and CF inputs into longer-lasting slow-output Ca^{2+} signals (29).

PF stimulation activates two signaling pathways. It triggers glutamate release at the synapse, which leads to an activation of type-1 metabotropic glutamate receptors (mGluR1) located at the postsynaptic density (PSD) at the top of the spine head. The activated mGluRs activate G-protein-coupled receptors (G_q) that cause the activation of phospholipase Cβ (PLCβ), which synthesizes IP_3 from PIP_2. IP_3 is free to diffuse from the PSD into the dendrite's cytosol (30–32) before it vanishes because of degradation by IP_3 3-kinase and IP_3 5-phosphatase on the timescale of a few seconds (33,34). The second pathway consists of a membrane depolarization, causing Ca^{2+} influx through voltage-gated Ca^{2+} channels ($Ca_v2.1$ type P/Q-voltage-gated Ca^{2+} channels), which are highly expressed in Purkinje dendrites (35,36).

CF stimulation also generates a membrane depolarization opening the same type of P/Q-voltage-gated Ca^{2+} channels, which leads to Ca^{2+} influx not only into the spine but also into the dendrite (27), summarized in Fig. 1 (1–5).

Whereas PF synapses are located at the head of a dendritic spine coupled to the PSD, CFs attach to the dendrite itself, creating synapses at the dendritic arbor in $\sim$2–3 μm intervals (37). One Purkinje cell is connected to up to 10^5 parallel fibers but to only a single climbing fiber (17).

It is assumed that the activity patterns of PFs attached to Purkinje cells in the cerebellum mediate fine control of movement and promote an increase in synaptic strength (LTP), whereas the activity patterns of CFs encode information about failure of such movement and can trigger a decrease in synaptic strength (LTD) when succeeding PF stimuli (38,39).

The endogenous Ca^{2+} binding proteins (buffers) calbindin D28k (Cb), parvalbumin (Pv), and calmodulin (CaM) are highly expressed in Purkinje cells (17,40,41). Their role is to shape Ca^{2+} transients occurring in the cytosol by setting their spatiotemporal parameters such as amplitude and decay time, which are crucial for successful information transmission on cellular level via signaling pathways (42–46).

Various brain disorders are associated with malfunctioning neuronal information processing which can be related to atypically functioning dendritic spines and IP_3Rs (46–50). Among them, cerebellar ataxia is a serious and heterogeneous neurological condition involving a loss of coordination of muscle movement (51). Most forms of cerebellar ataxia have no cure to this day (52). Thus, it is important to develop computational models to study the role of dendritic spines with respect to ataxia (53). To model ataxia in our approach, we look at Ca^{2+} transients under reduced IP_3 binding rates of IP_3Rs and then suggest ways to restore previous Ca^{2+} transients.

Please cite this article in press as: Friedhoff et al., Stochastic reaction-diffusion modeling of calcium dynamics in 3D dendritic spines of Purkinje cells, Biophysical Journal (2021), https://doi.org/10.1016/j.bpj.2021.03.027

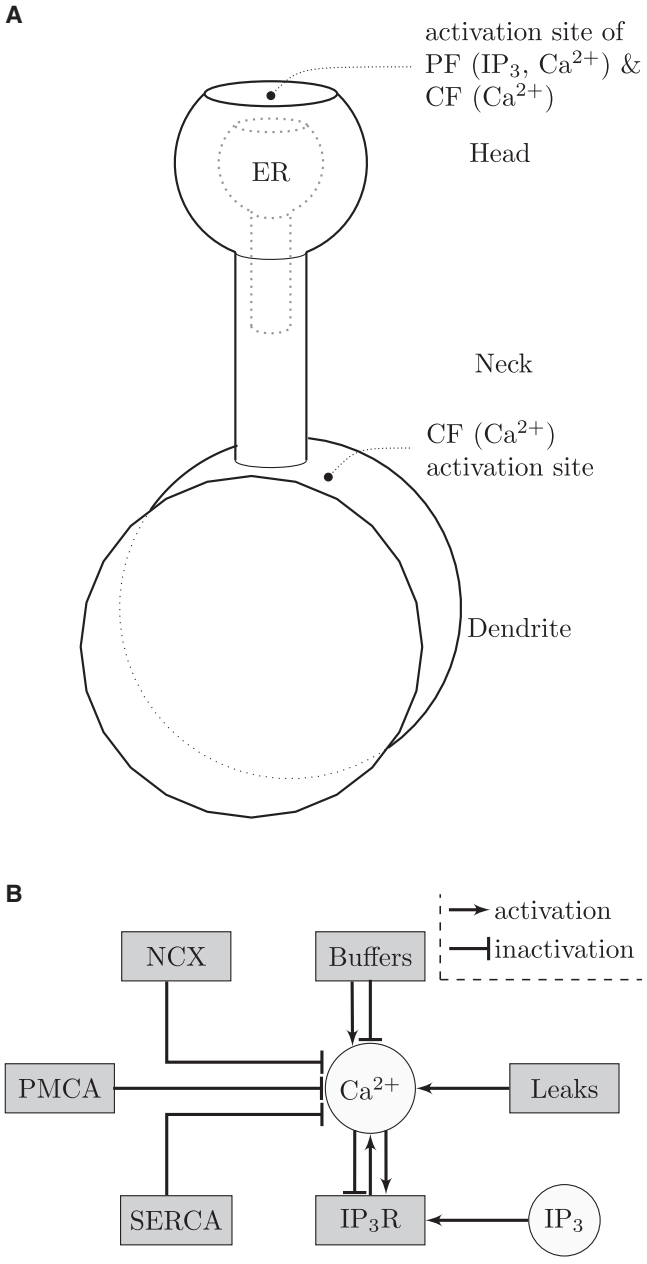

FIGURE 2 (*A*) Model geometry. The endoplasmic reticulum (ER) is visible in the head and neck. $V_{total} = 0.512\ \mu m^3$, $V_{head} = 0.100\ \mu m^3$, and $V_{ER} = 0.020\ \mu m^3$. Release sites of Ca^{2+} and IP_3 for PF and Ca^{2+} for CF activation are marked by dots. Exact sizes of the geometry can be found in Table S4. (*B*) Interaction scheme of particle species used in the simulations from a cytosolic perspective. SERCAs, leak channels, and IP_3Rs are located on the ER membrane, and PMCAs, NCXs, and more leak channels are located on the outer plasma membrane. Ca^{2+}, IP_3, and the buffers are free to diffuse in the cytosol, the volume within the plasma membrane, and outside the ER.

METHODS

Model description

The model studies the Ca^{2+} response to outer stimuli from active PFs and CFs. Simulation methods are explained in the Supporting materials and methods. Stochastic reaction-diffusion, particle-based simulations use MCell (54–56), and deterministic simulations use Copasi (57). Whereas MCell offers a biophysically realistic approach to a biological problem, accounting for low particle concentrations, inherent stochasticity, and complex three-dimensional geometries (58), Copasi describes the kinetic reactions in a well-mixed volume efficiently, without the influence of diffusion or complex geometry. In this way, the dynamics of the model can be tested in a computationally fast environment before going into more expensive reaction-diffusion simulations in complex geometries. Copasi was, for instance, used to approximately find concentrations of each species at equilibrium, i.e., the initial state then used for simulations in MCell. We focus on explaining model components here. All parameter values not mentioned explicitly in the text are listed in the Supporting materials and methods.

Geometry

We created the simple three-dimensional dendrite-neck-head volume shown in Fig. 2 *A* for our MCell simulations. The head consists of a sphere with the top and bottom being cut off. The top area models the PSD, and the bottom of the sphere connects to the spine's cylindrical neck. A cylindrical dendrite is attached to the other side of the neck. The head volume is $V_{head} = 0.1\ \mu m^3$. The total volume dendrite, neck and head, is ~5 times as large, $V_{total} = 0.512\ \mu m^3$ (59).

We created another volume inside the head and neck to represent the smooth ER. It is a scaled copy of the head and neck, just smaller in size, with $V_{ER} = 0.02\ \mu m^3$. Although the surface of the ER is home to IP_3Rs, ER Ca^{2+}-ATPases (SERCAs), and leak channels, we did not model the inside of it. For Ca^{2+} release by IP_3Rs, we assume a constant Ca^{2+} efflux (60) on the timescale of interest not affected by ER depletion. We are aware of this being an approximation because ER depletion is suggested by the results of Okubo et al. (61), with intralumenal diffusion as the major flux of replenishment. However, lumenal concentrations, together with the ER size required to account for lumenal diffusion on the timescale of release, would render our study unfeasible because of particle numbers above 2×10^5.

Additionally, we used no-flux boundary conditions at the dendrite sites for all particle species, modeling a situation in which neighboring spines also receive stimuli (see (62), their Fig. 1 *b*).

Molecular components of Ca^{2+} dynamics

General and steady-state particle concentrations, number of particles, and diffusion coefficients can be found in Tables S5 and S6.

Ca^{2+} transporters

SERCA pumps are described by a three-state model (63,64), Fig. S3 and Table S4, subsequently binding two Ca^{2+} before decaying back into the rest state, removing two Ca^{2+} from the cytosol. We put 68 SERCAs onto the ER membrane (64).

We included five sodium-calcium exchangers (NCXs) (63,64) on the outer plasma membrane without modeling sodium dynamics. Our model assumes constant intracellular and extracellular $[Na^+]$ as a simplification. We used a simple two-state model (64), i.e., one NCX receptor can bind one Ca^{2+} and then either release it back into the cytosol or decay back into the rest state, removing one Ca^{2+}.

Plasma membrane Ca^{2+}-ATPase (PMCA) is another Ca^{2+} pump that helps to maintain a low Ca^{2+} concentration in the cytosol of all eukaryotic cells. We used 13 PMCAs (63,64) and also a two-state model similar to the NCX model, but with different reaction rates (65,66).

We include 10 leak channels on each the ER and plasma membrane of the dendrite that yield a small constant influx of Ca^{2+} into the cytosol. The leak fluxes fix free $[Ca^{2+}] \approx 50$ nM in steady state.

Buffers. The buffer species in the model are Pv, Cb, and CaM (Fig. 3). We describe Pv by a three-state model. It binds either one Ca^{2+} or one magnesium (Mg^{2+}) (42,67).

Please cite this article in press as: Friedhoff et al., Stochastic reaction-diffusion modeling of calcium dynamics in 3D dendritic spines of Purkinje cells, Biophysical Journal (2021), https://doi.org/10.1016/j.bpj.2021.03.027

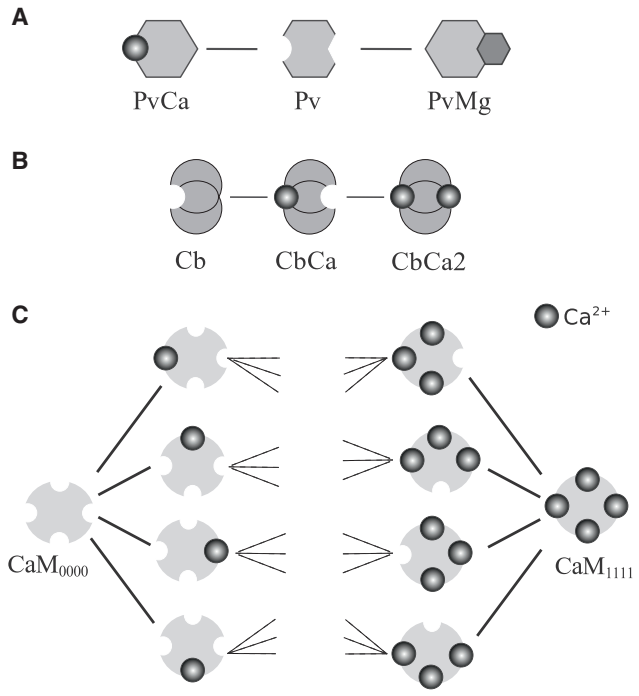

FIGURE 3 Overview of buffer models for (*A*) Pv, (*B*) Cb, and (*C*) CaM. CaM can hold up to four Ca^{2+}. We used a 16-state model with individual binding sites. For ease of reading, we omitted the six states with two bound Ca^{2+}. Reaction rates for all can be found in Table S3.

Cb is a major Ca^{2+} buffer in spines of hippocampal and also Purkinje neurons. We used a three-state kinetic model with a low- and a high-affinity site (42,68), with the low-affinity site being present only if the high-affinity site is filled. One Cb protein can therefore bind up to two Ca^{2+}.

CaM is a multifunctional calcium-binding protein expressed in all eukaryotic cells. It is not only a buffer but also acts as a messenger target of Ca^{2+}. Once Ca^{2+} is bound to CaM, it can modify the interactions of Ca^{2+} with various other targets like phosphatases or kinases. One CaM protein has four Ca^{2+} binding sites. We modeled the interactions with Ca^{2+} using a 16-state model with various medium- and high-affinity binding sites and various reaction rates (66).

IP_3R models

We used 54 or 56 IP_3Rs (69) on the ER membrane, depending on the parameter set. A large variety of IP_3R models have been developed in the last three decades (70–73). We compare here two models. Doi's model has been chosen because it has been applied to spine dynamics before (63). We picked Moraru's model for comparison because its open probability depends nonlinearly on [Ca^{2+}], and it is eligible for easy implementation in MCell (74). This choice allows for statements on the role of IP_3R inhibition and IP_3R-related slow timescales.

Doi's model. A seven-state model for the IP_3R was proposed by Doi et al. (63). The model is able to reproduce the bell-shaped open probability curve $P_0([Ca^{2+}])$ (Fig. 4 *C*). An IP_3R requires one IP_3 to bind before one Ca^{2+} binds to open; otherwise, it will stay closed and can only bind more Ca^{2+} if it does not previously release the bound Ca^{2+}. Once the receptor opens, it releases Ca^{2+} into the cytosol with a constant Ca^{2+} release rate (Figs. 4 *A* and S2; Table S2).

Moraru's model. We chose a subsection of the IP_3R model of Moraru et al. (74), in which we ignored an additional slow IP_3 binding site that is irrelevant for the timescales considered in our model. An IP_3R can maximally bind four Ca^{2+} and four IP_3 molecules, and any state transition that includes binding or unbinding of one Ca^{2+} or one IP_3 is allowed. There is an additional transition from the state T_{42} with four bound IP_3 (75) and two bound Ca^{2+} to the open state, T_{open}. Moraru's model also reproduces the bell-shaped open probability curve (Fig. 4 *C*). The amplitude of the open probability is easily controlled by changing the reaction rates k_{open} and k_{close} of the transitions between T_{42} and T_{open} (Fig. S1). Because it is known that the binding dynamics of inhibitory Ca^{2+} is slower than that of excitatory Ca^{2+} by a factor of up to 100 (70,76), we decreased the inhibitory Ca^{2+} binding reaction rates into and from states T_{x3} and T_{x4}, which represent the inhibitory Ca^{2+} binding sites in this model, by an additional factor r_s (see Fig. 4 *B*; Table S1).

Parallel and climbing fiber stimulation

We studied the Ca^{2+} response to four different types of stimuli after experimental results (8): a single PF stimulus, PF burst, CF stimulus, and PF burst + CF stimulus. Stimulation by active PFs was simulated by plasma membrane influx of Ca^{2+} and IP_3 production close to the PSD. CF stimulation was modeled by Ca^{2+} influx close to the PSD and into the dendrite end close to the spine neck (Fig. 2).

We chose different amounts of Ca^{2+} per PF and CF stimuli (0–1500 Ca^{2+} and 0–2000 Ca^{3+}, respectively) as part of our parameter scan. A single PF stimulus consists of one instantaneous injection of Ca^{2+} and production of IP_3 (380 close to the PSD), and a PF burst was made up of five single Ca^{2+} injections at 100 Hz and 1400 caged IP_3, yielding an ~5 times larger IP_3 transient. In the latter, more relevant case, free [IP_3] usually peaks around 4.5–5 μM. A CF stimulus included an additional Ca^{2+} release of 200 particles in the dendrite (Fig. 1). The typical time of the CF stimulus is t_{CF} = 100 ms after the initiation of the PF stimuli but was varied in Optimal timing of CF stimulus.

IP_3 dynamics used constant production and decay rates and was able to capture biexponential IP_3 concentration behavior (33,34,63,77). We chose an amount of IP_3 in agreement with physiological concentrations (6) such that the IP_3Rs were saturated with IP_3 for the case of a PF burst. IP_3 production was delayed by 100 ms compared to the onset of the PF Ca^{2+} influx to account for the slower process of IP_3 synthesis compared to instantaneous Ca^{2+} influx from PF and CF stimuli. IP_3 diffuses freely in our model.

RESULTS

We successfully constructed a three-dimensional stochastic reaction-diffusion model of Purkinje cell dendritic spine Ca^{2+} dynamics that reproduces many aspects found in experiments (8,62). Because of the nature of computational modeling, we were able to shed light on some aspects of the system's response to stimuli that are otherwise extremely hard to control experimentally, e.g., removing certain buffer species or changing the amplitude of Ca^{2+} associated with a PF or CF stimulus.

Snapshots of the spine head including Ca^{2+}, IP_3, and IP_3R states on the ER from a typical simulation are shown in Fig. 5. At t = 0 ms in the first frame, the red dot is the initially localized collection of 110 Ca^{2+} of the first PF stimulus. The particles diffuse and get absorbed by buffers immediately. The CF stimulus consists of 1700 Ca^{2+}, which is visible in three frames corresponding to t = 100 ms to t = 100.032 ms, showing how quickly Ca^{2+} diffuses. IP_3 slowly enters the system at the same time at t = 100 ms (see also Fig. 9 *A*). IP_3Rs start to react to IP_3 and increased [Ca^{2+}] (note changing colors of IP_3Rs). Eventually, a global Ca^{2+} transient is initiated, which leads to a prolonged increase

Please cite this article in press as: Friedhoff et al., Stochastic reaction-diffusion modeling of calcium dynamics in 3D dendritic spines of Purkinje cells, Biophysical Journal (2021), https://doi.org/10.1016/j.bpj.2021.03.027

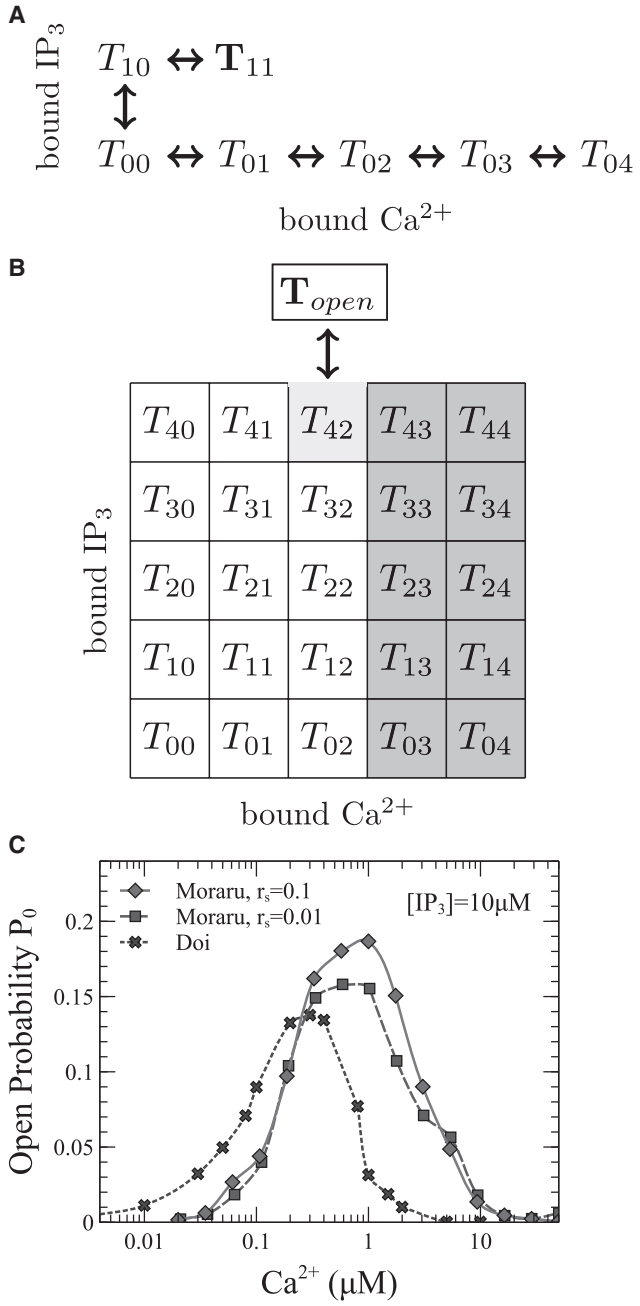

FIGURE 4 (*A*) Doi's model: T_{00} represents an empty IP_3R. The IP_3R acts as a coincidence detector and only opens if IP_3 binds before Ca^{2+}, making T_{11} the open state. Otherwise, it buffers Ca^{2+} and becomes inactivated, preventing binding of IP_3. (*B*) Subsection of Moraru's model. All vertical and horizontal transitions are possible. When four IP_3 and two Ca^{2+} (activating) are bound, T_{42} (*light gray*), there is a probability to go into the open state T_{open}, whence additional Ca^{2+} will be released. Further Ca^{2+} binding of the IP_3R will lower the probability of opening, effectively promoting the 10 states T_{x3} and T_{x4} to inhibitory Ca^{2+} states (*gray*), $x \in [0, 4]$. We set the Ca^{2+} binding and dissociation rates of the inhibitory states to be slower than the rates of the activating states, expressed by ratio r_s. Parameter values can be found in Table S1. (*C*) IP_3R open probability at constant $[IP_3] = 10$ μM for Doi's (*dotted*) and our version of Moraru's model with inhibitory Ca^{2+} binding scaling $r_s = \{10^{-1}, 10^{-2}\}$ (*dashed* and *solid*, respectively). Data points are results of stochastic computations with Copasi. The rise of the open probability at low Ca^{2+} causes CICR.

of $[Ca^{2+}]$, shown from t = 350–650 ms (see also Fig. 6). Using many of these simulations, we studied the IP_3-induced Ca^{2+} responses of our model spine to different stimuli. We chose these stimuli in accordance with available experimental data (8,62). We were able to approximately reproduce properties of Ca^{2+} transients in the spine head in response to a PF, CF, PF burst, and PF burst + CF stimulus when using Moraru's IP_3R model, as we will see below.

We focused on the difference of Ca^{2+} transients, especially on the peak values, upon a PF burst and a PF burst with a CF stimulus coactivation at $t_{CF} = 100$ ms after the onset of the PF burst, as these two cases are assumed to encode the induction of LTP and LTD, respectively (38,39,45). We expect the system to show a clear Ca^{2+} transient with a spine head peak of $\sim$2.8 μM under a PF burst stimulus and a 150% increase to $\sim$7.1 μM with a CF coactivation (8), showing a supralinear response to summation of stimuli, also generally found in other model approaches (29,63,78) and experiments (44,62).

Robustness of IP_3R dynamics against Ca^{2+} concentration noise: a model with linear activation characteristics

Local concentration fluctuations at IP_3Rs upon opening or closing are large (79,80), and therefore, channel state noise strongly affects channel state dynamics. In this section, we investigate the noise response of linear Ca^{2+}-dependent channel activation in the IP_3-sensitized state as, e.g., Doi's model uses. We and others (63) were able to reproduce dendritic spine Ca^{2+} dynamics in well-mixed conditions with Doi's model as a system of ordinary differential equations (ODEs), generating proper Ca^{2+} transients to different PF and CF stimuli conditions (see also Figs. S6 and S7).

We found with MCell simulations that the stochastic fluctuations of Ca^{2+} in the cytosol prevent any possible rise of the Ca^{2+} transient peak with CF or PF stimuli with linear Ca^{2+}-dependent IP_3R channel activation. It takes only one Ca^{2+} to bind to the receptor to open if sufficient IP_3 is already present. Once one or two IP_3Rs are in the open state just because of basal Ca^{2+} fluctuations, they release enough Ca^{2+} to open more IP_3Rs to create a global Ca^{2+} transient with a peak $\sim$ 3.0 μM (Fig. S5 *A*). Adding more Ca^{2+} because of PF (Fig. S5, *B–D)* or CF (Fig. S5 *E)* stimuli did not show any further peak increase because the transients arising from basal fluctuations are saturated already. Even large CF Ca^{2+} amplitudes left the Ca^{2+} peak values essentially unchanged. The peaks of the Ca^{2+} transients are essentially constant for Ca^{2+} PF amplitudes 0–220 (Fig. S5 *F*). At large PF amplitudes (>220 Ca^{2+}), the inhibitory action of Ca^{2+} on the IP_3Rs decreased transient amplitudes significantly, as some of the total available IP_3Rs bind inhibitory Ca^{2+} before a global transient can be initiated. Results from adding a CF stimulus with increasing CF Ca^{2+} amplitude are shown in Fig. S5 *F,* in which a small peak decrease is visible.

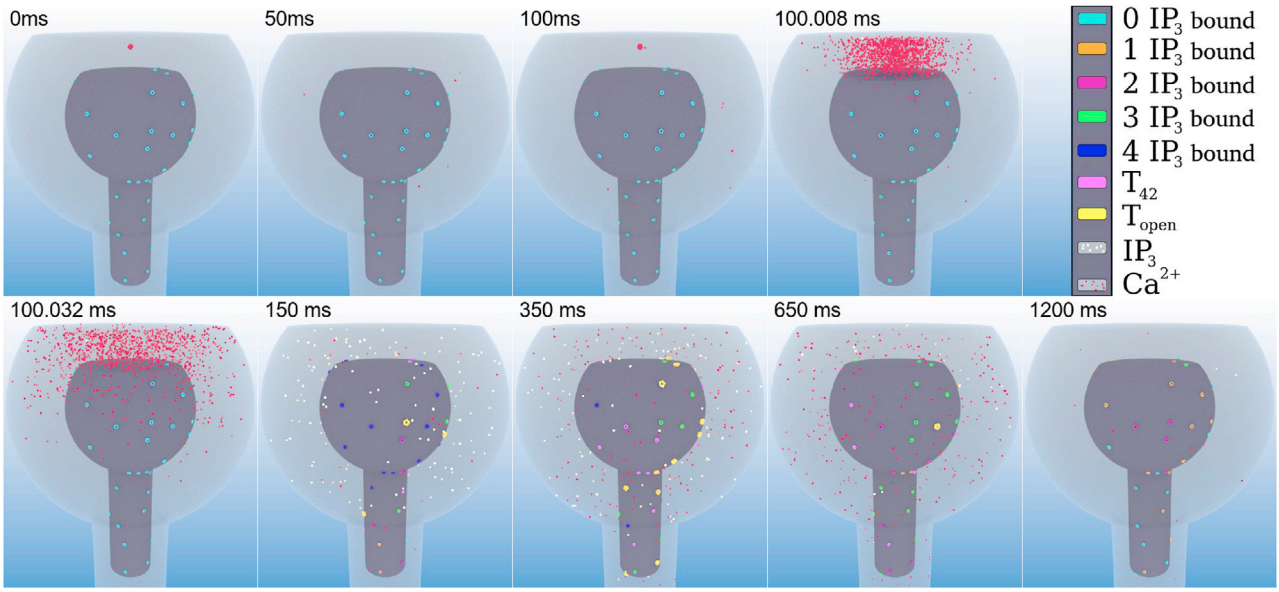

FIGURE 5 Snapshots of the spine head from a typical simulation with Ca^{2+} (*red*), IP_3 (*beige*), and IP_3Rs colored according to their state (Moraru's model) as explained by the legend. At t = 0 ms, the large red dot shows the 110 Ca^{2+} coming from the first PF stimulus, and at t ≈ 100 ms, 1700 Ca^{2+} from the CF stimulus. The highly localized Ca^{2+} stimuli very rapidly spread by diffusion and are absorbed by buffers. Spatial averages of the Ca^{2+} concentration are shown in Fig. 6. To see this figure in color, go online.

This high sensitivity to noise of IP_3Rs in this model has not been observed in stochastic simulations based on molecule numbers only, i.e., in non-spatially-resolved simulations (81). Given the same molecule number amplitude, the local concentration amplitude of fluctuations in our spatially detailed simulations is larger than in the spatially lumped simulations of Koumura et al. (81). This effect of local noise most likely explains the different results with respect to noise sensitivity (14,15,82) and renders spatially resolved simulations necessary (83).

Therefore, we turn to a model with nonlinear Ca^{2+}-dependent activation characteristics in the following.

Moraru's IP_3R model

A model with nonlinear Ca^{2+}-activation characteristics like Moraru's model exhibited better robustness against basal fluctuations, and we use it from now on.

Ca^{2+} transient peak response to a PF and CF stimulus

Piochon et al. (8) estimated the peak of the Ca^{2+} transient in the spine head after a single PF stimulus paired with a CF stimulus to be ∼0.4 μM, whereas the response to a single PF stimulus was lost in noise. More interestingly, a PF burst stimulus triggered a Ca^{2+} response with a peak value of ∼2.8 μM, and a peak value of ∼7.1 μM was reached for a PF burst stimulus with CF coactivation, an increase of ∼150%. Ca^{2+} peak increase with CF coactivation is crucial for the current understanding of initiation of synaptic plasticity in the form of long-term depression (LTD) (9,17), even though LTD has also been observed after very strong PF stimulation alone (8,26,84,85).

We were able to reproduce Ca^{2+} transients with peak values in agreement with experimental data for the cases of single PF with additional CF coactivation, PF burst, and PF burst with CF coactivation. Summarized Ca^{2+} results from our simulations for some example parameter sets are shown in Fig. 6 *A*, where the peak of the Ca^{2+} transients in response to a PF burst and a PF burst + CF stimulus are shown. The peak values of Ca^{2+} transients computed deterministically in Copasi increased clearly with increasing PF and CF Ca^{2+} amplitudes and showed no saturation for tested parameters. The system was very sensitive to CF coactivation (see Figs. S8 and S9).

Averages and the standard deviation (SD) of actual transients of Ca^{2+} are shown in Fig. 6 *B*. The SD due to the inherent randomness is large but does not blur the difference between a single PF burst and combined PF burst + CF stimulus.

We simulated a single PF stimulus with CF coactivation and obtained an average peak value of ∼20 Ca^{2+} = 0.40 μM from 12 simulations, in agreement with Piochon et al. (8) (Fig. S12).

Closing of IP_3Rs was caused by a mixture of reaching the inhibitory states T_{x3} and T_{x4} with three or four Ca^{2+} bound for larger values of r_s due to increasing [Ca^{2+}] during a Ca^{2+} transient (see *bell-shaped open probability curve*, Fig. 4) and IP_3 becoming less available during IP_3 degradation; see IP_3R state occupation videos (Videos S1, S2, S3, and S4) with different values of r_s in the Supporting material.

Please cite this article in press as: Friedhoff et al., Stochastic reaction-diffusion modeling of calcium dynamics in 3D dendritic spines of Purkinje cells, Biophysical Journal (2021), https://doi.org/10.1016/j.bpj.2021.03.027

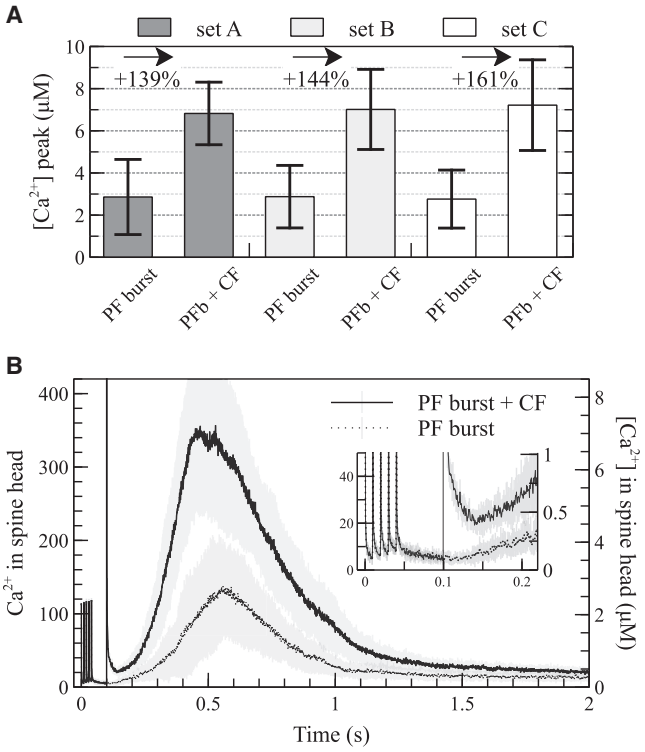

FIGURE 6 (*A*) Moraru's model: peak values of Ca^{2+} transients in the spine head for different parameter sets to PF burst and PF burst + CF (PFb + CF) stimuli, averaged over 12 simulations. Error bars show SDs. Parameters are A, N = 54 IP_3Rs, PF = 90 Ca^{2+}, and CF = 1700 Ca^{2+}; B, N = 54 IP_3Rs, PF = 150 Ca^{2+}, and CF = 1700 Ca^{2+}; and C, N = 56 IP_3Rs, PF = 110 Ca^{2+}, and CF = 1700 Ca^{2+}. Set C is our control parameter set and will be used from now on. (*B*) Ca^{2+} in spine head after PF burst (*dotted*) and PF burst + CF (*solid*) stimuli with control set. The inset shows a magnification of the first 220 ms. At t = 0.1 s, the highly localized Ca^{2+} from the CF stimulus is visible as a spike. The injected Ca^{2+} gets absorbed by buffers immediately explaining the immediate return to lower [Ca^{2+}] shortly after the stimulus. The averages with SDs (*greyish areas*) of 12 simulations are shown.

During a typical Ca^{2+} transient, [Ca^{2+}] stays approximately constant in the spine head, decreases linearly down the neck and becomes constant again in the dendrite segment of the volume, see Video S5.

Results of Ca^{2+} transients to different stimuli conditions and associated total Ca^{2+} release from IP_3Rs with single buffer species removed, showing how single buffer species shape Ca^{2+} transients and influence IP_3R dynamics, are presented in Fig. S11.

Ca^{2+} transient peak scaling with PF and CF Ca^{2+} amplitude

We find that the relation between the peak value of Ca^{2+} transients and the CF Ca^{2+} amplitude is strongly affected by the rate of Ca^{2+}-dependent inhibition of the IP_3Rs (Table S1). The rate value suggested in the original Moraru model entails saturation at a CF Ca^{2+} amplitude of 500 already (*diamonds* and fit with $r_s = 1.0$ in Fig. 7 *A*). Peak values increase with CF amplitude over a large range with a smaller rate of inhibitory Ca^{2+} binding to the IP_3R, r_s. We find measured responses of the transient peak to a CF stimulus coactivation and beyond with even larger CF amplitudes with $r_s = 0.01$ (*circles*, Fig. 7 *A*). We used this value throughout the study. The same applies to the response to PF stimuli with various Ca^{2+} amplitudes, showing larger peak values for smaller r_s (Fig. 7 *B*). Additionally, increasing PF Ca^{2+} amplitudes (without CF coactivation), mimicking a situation of intense PF stimulation, increases peak values even further, reaching the same or even higher peak values than with CF coactivation and smaller PF Ca^{2+} amplitudes in Fig. 7 *B*. This resembles the situation in which a strong PF stimulus alone, rather than PF stimulation with CF coactivation, can trigger LTD (8,26,84,85).

Optimal timing of CF stimulus

The size of the Ca^{2+} transient elicited by the CF stimulus, and with it the induction of LTP and LTD, responds optimally to a certain timing of the CF stimulus relative to the PF stimulus as Wang et al. have shown (62). They measured the Ca^{2+} response to different timing windows between CF and PF stimulus and used a Gaussian to fit the Ca^{2+} transient's total integrated response to their results, which peaked around 92 ± 37 ms and had a half-width of 212 ± 85 ms.

We simulated these experiments by varying the CF stimulus time from 0 to 400 ms after the initiation of the PF stimulus. We find that the system is sensitive to the timing of the CF stimulus, as shown when determining the Ca^{2+} transient peaks under such CF Ca^{2+} timing variation and also exhibits optimal time windows with a maximal peak (Fig. 8). We find optimal responses for different strengths of PF stimuli also including the parameter value set A in Fig. 6.

We compare our results in Fig. S10 to the experimental data from Wang et al. (62).

The rising phase of the Ca^{2+} peaks in Fig. 8 is due to Ca^{2+}-induced Ca2 release (CICR) (see Fig. 4 *C*). The CF stimulus causes Ca^{2+} influx. It takes more than 200 ms for this Ca^{2+} rise to decay back close to prestimulus levels (Figs. 6 and S12). When IP_3 production starts 100 ms after onset of PF stimulation, CICR starts because of the presence of IP_3 and the remaining Ca^{2+} from the CF stimulus. The closer to IP_3 production the CF stimulus occurs, the stronger the CICR. Interestingly, this does not necessarily lead to an optimal response at a timing window at the time of onset of IP_3 production at 100 ms, as the blue and green curves in Fig. 6 show. We did not observe optimal time windows when we released IP_3 at the onset of PF stimulation (data not shown).

The decaying phase of the Ca^{2+} peaks in Fig. 8 toward large time windows is affected by processes terminating Ca^{2+} release. One of them is the decay rate of IP_3 as the

Please cite this article in press as: Friedhoff et al., Stochastic reaction-diffusion modeling of calcium dynamics in 3D dendritic spines of Purkinje cells, Biophysical Journal (2021), https://doi.org/10.1016/j.bpj.2021.03.027

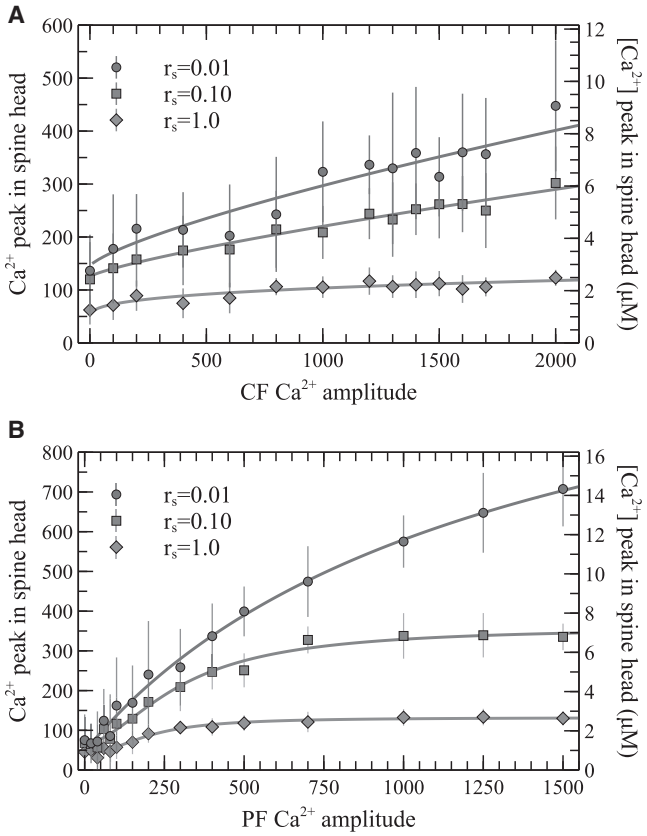

FIGURE 7 Peak scaling of Ca^{2+} transients against (*A*) CF Ca^{2+} amplitude for the PF burst + CF scenario and (*B*) against PF Ca^{2+} amplitude for the PF burst scenario for three different inhibitory Ca^{2+} binding timescale ratios $r_s = \{1.0, 0.1, 0.01\}$; see Table S1. The slower the rate of inhibition, the larger the resulting Ca^{2+} transients for a given CF or PF Ca^{2+} amplitude. The value of r_s sets the largest possible peak value when varying PF and CF Ca^{2+} amplitudes. Large enough transients triggered by CF coactivation with intermediate Ca^{2+} amplitudes are only reached when r_s is on the order of 10^{-2}. Data points are averages of 12 stochastic simulations and were fitted to Hill curves, error bars show SDs.

simulations in Fig. 9 show (which we will discuss in more detail below). The slower IP_3 is removed from the spine head—either by degradation or by diffusing out of the spine—the longer the Ca^{2+} transient.

Ca^{2+}-dependent inhibition is another process contributing to the termination of Ca^{2+} release and affecting the peak dependency on the CF time window as the comparison between the purple curve and all other ones in Fig. 8 shows. Additionally, the peak scaling data in Fig. 7 illustrate the role of Ca^{2+}-dependent inhibition in setting peak height. Increasing the rate of Ca^{2+}-dependent inhibition leads to a longer time window providing optimal response (*purple curve* in comparison to the *blue one*).

However, increasing the inhibition rate by a factor of three does not shorten the Ca^{2+} transient by the same factor and does not abolish optimal time windows because Ca^{2+}-dependent inhibition is only one of several factors shaping the transient.

Ataxia

It has been shown that spinocerebellar ataxia type 29 (SCA29), characterized by early-onset motor delay, hypotonia, and gait ataxia, can be caused by malfunctioning type 1 IP_3Rs (50). Mutations associated with SCA29 were identified within or near the IP_3-binding domain. These mutations interfere with the binding of IP_3 and cause IP_3Rs of type 1 to lose any channel activity, reducing or removing IP_3-induced Ca^{2+} transients.

On that basis, we decrease the IP_3 binding rate k_{on} of the IP_3R model to mimic ataxia, which results in lower or vanishing Ca^{2+} transients. We search to rescue the system from this pathological condition by trying to recover the original Ca^{2+} peak in two ways. First, we increase the amount of IP_3 that enters the system, representing increased activity of the PLCβ pathway, which synthesizes IP_3. In a second approach, we decrease the degradation rate of IP_3, thus increasing the IP_3 that is available to the IP_3Rs in absolute number as well as in duration.

The first method of increasing IP_3 was only able to recover the Ca^{2+} transients if we increased the amount of IP_3 like $1/k_{on}$ (see Fig. S13). Because the decrease of k_{on} might be substantial (50), the $[IP_3]$ values compensating it are likely beyond the saturation values of the PLCβ pathway.

Prolonging IP_3 exposure

We decrease the IP_3R's binding rate of IP_3 to values possibly representing ataxia and then reduce k_{decay} trying to recover the original Ca^{2+} transient. We start from their standard values $k_{on} = 83.3\ (\mu M\ s)^{-1}$ and $k_{decay} = 15\ s^{-1}$.

The control Ca^{2+} peak value can be recovered because slower IP_3 degradation increases the amount and duration of IP_3 in the system (Fig. 9 *A*), making up for the negative effects of slower IP_3 binding. Additionally, the decrease of k_{decay} leads to prolonged activity of the open IP_3R. The slowed IP_3R dynamics also cause some delay in reaching the Ca^{2+} peak (Fig. 9 *C*). Whereas the control parameters yield a Ca^{2+} transient peak at ~0.47 s (*red*, Fig. 9 *C*), slowing IP_3 degradation down to one-sixth $k_{decay} = 2.5\ s^{-1}$ delays the peak to ~0.65 s (*orange*), i.e., it increases the response time by ~40% and increases the width of the Ca^{2+} transient.

We provide a more systematic analysis in Fig. 9 *B*. It shows the peak values in dependence on k_{on} for five different IP_3 decay rates k_{decay}. The red curve shows results with the control value of k_{decay}. The curves with reduced k_{decay} cross the Ca^{2+} peak control value 360 (*red dotted line*) at specific values $k_{on,\ ax}$, which are smaller than the k_{on} control value. They are related to k_{decay} approximately by $k_{decay} \approx \frac{k_{on,ax}}{6.0\mu M^{-1}}$. Simulations with the parameter value pairs of (k_{decay}, $k_{on,\ ax}$) calculated according to this equation provide control of Ca^{2+} peak values with our control parameter set for all other parameter values. A decay rate reduction calculated according to this equation compensates the pathological reduction of $k_{on,\ ax}$ with respect to the Ca^{2+} transient peak.

Please cite this article in press as: Friedhoff et al., Stochastic reaction-diffusion modeling of calcium dynamics in 3D dendritic spines of Purkinje cells, Biophysical Journal (2021), https://doi.org/10.1016/j.bpj.2021.03.027

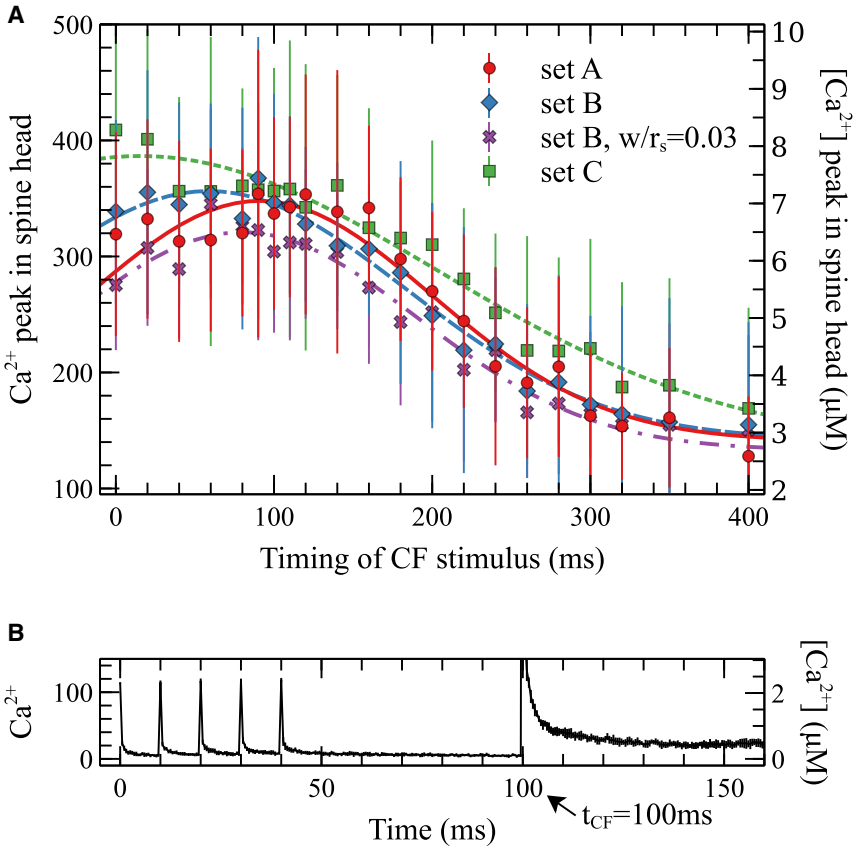

FIGURE 8 (*A*) Peak of Ca^{2+} transients against timing of CF stimulus for three parameter sets from Fig. 6 and an additional one with $r_s = 0.03$. 12 stochastic simulations per data point were used, and points were fitted to Gaussians with the condition to converge against peak values of PF burst stimulation alone for very large and small t_{CF}. Error Bars indicate SDs. The maxima of the Gaussian fits occur at 91 ms (*red*), 59 ms (*blue*), 16 ms (*green*), and 80 ms (*purple*), in qualitative agreement with experimental data (62) (+92 ± 37 ms). The half-widths of the Gaussian fits are 257 ms (*red*), 294 ms (*blue*), 443 ms (*green*), and 260 ms (*purple*), in qualitative agreement with experimental data (62) (212 ± 85 ms). (*B*) Illustrating PF and CF stimulus timing by showing five Ca^{2+} spikes in spine head from a PF burst stimulus at 100 Hz from 0 to 40 ms and a Ca^{2+} spike from a CF stimulus, here $t_{CF} = 100$ ms. To see this figure in color, go online.

DISCUSSION

Cerebellar learning theories suggest that learning is expressed as a change of neuronal weights, i.e., synaptic strengths, reflecting the topological properties of a neuronal network state. Understanding learning therefore requires knowledge of the molecular mechanisms assumed to encode synaptic plasticity and information transmission at the lowest neuronal level, which are Ca^{2+} transients and the associated cell responses in synapses of spines, eventually. In Purkinje neurons, the IP_3-induced Ca^{2+} transients are dynamical responses to outer stimuli from PFs or CFs happening at low Ca^{2+} concentrations. Whereas PFs are assumed to carry information about movement and fine motor control, CFs are assumed to carry error information that gives feedback about the network state that triggered the movement (86–88). We developed a model that is based on complex single-particle stochastic reaction and diffusion processes within a small three-dimensional geometry to study Ca^{2+} transients in response to dynamical PF and CF stimuli.

Our use of three-dimensional stochastic simulations demonstrated the necessity for IP_3R models to filter out Ca^{2+} binding noise to a sufficient degree. A linear relation between $[Ca^{2+}]$ and the open probability at small concentrations appears not to provide that filtering and entailed Ca^{2+} dynamics insensitive to CF and PF stimulus Ca^{2+} amplitudes. However, an increase of the Ca^{2+} transient peak due to a CF stimulus provides meaning to this stimulus and is thus a necessary model requirement.

Using Moraru's IP_3R model to provide sufficient noise filtering, we were able to reproduce the dynamic behavior of the Ca^{2+} transients from experiment with respect to the absolute and relative peak values of Ca^{2+} transients under stimuli (8) and the behavior of peaks under variation of the timing of the CF stimulus (62).

The signal of the CF stimulus turning LTP into LTD might be binary information or graded information. If simply the presence of a stimulus entails LTD, we face binary signaling. If the strength of the stimulus encodes the strength of depression, we see a graded response. We found this characteristic of the signaling by the CF stimulus to depend on the rate of Ca^{2+}-dependent inhibition of the IP_3R. We achieved agreement of Ca^{2+} transient peak values with experimental results at slow inhibition rates. Although these rates are slower than originally suggested by the authors of the model, they are still compatible with puff data of the IP_3R taking the large local $[Ca^{2+}]$ at puff sites into account (79,89,90). In summary, these simulation results suggest a graded response of the Ca^{2+} transients' peak value to the CF Ca^{2+} amplitude.

Using our model also allowed for detailed tests on the effects of endogenous Ca^{2+} buffer molecules. We find clear indication that buffers do not only passively shape

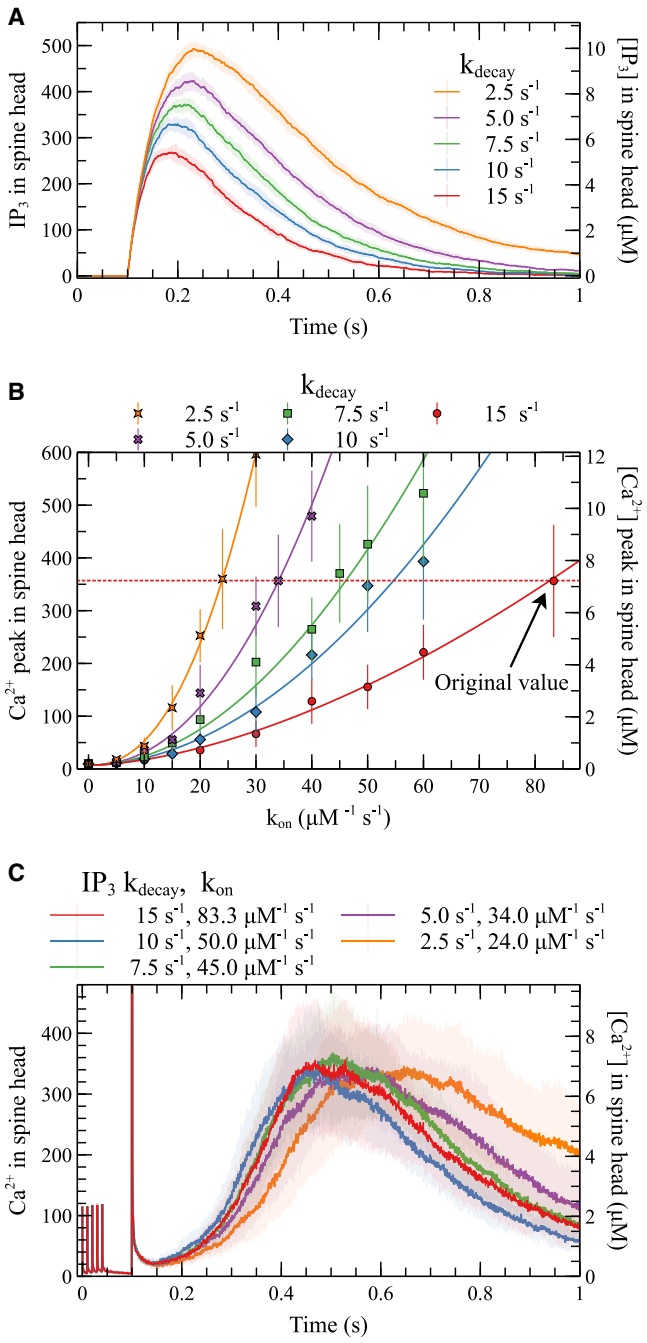

FIGURE 9 (*A*) Time courses of average $[IP_3](t)$ and SDs in the spine head for different IP_3 decay rates are shown. (*B*) Data points show averages of Ca^{2+} peak values and SDs for different values of IP_3 decay rates k_{decay} against the binding rate of IP_3. Each color and fit represent one decay rate. Binding rates smaller than the original value possibly represent ataxia. (*C*) Averages of 12 Ca^{2+} transients and SDs for cases with modified IP_3 decay and binding rates, taken from (*B*), that approximately peak around the original peak value of 360 Ca^{2+} (*dotted red line* in (*B*)) are shown. To see this figure in color, go online.

amplitude and decay and rise times of Ca^{2+} transients but actively modulate state dynamics of IP_3Rs, resulting in an increase or decrease of released Ca^{2+}.

It has been experimentally established that the timing window of PF and CF stimuli is critical to the induction of LTP and LTD and thereby also to the properties of the IP_3R-induced Ca^{2+} transients (62). The mechanism our results suggest is that the relative timing of IP_3 production elicited by PF stimuli, which sensitizes IP_3Rs for CICR to the moment of the influx of Ca^{2+} due to the CF stimulus causing CICR, sets the optimal time window.

We simulated ataxia on the basis of the assumption that it manifests itself in our model by a substantially reduced rate of binding of IP_3 to the IP_3R. Reducing the rate of IP_3 degradation by IP_3 3-kinase and IP_3 5-phosphatase turned out to be able to compensate the reduced binding without strong stimulation of the PLC pathway. Whether the recovered peak values are enough to trigger an increase of AMPA receptors in agreement with observations by Piochon et al. (8), even with delayed peak times and decay of the Ca^{2+} transients, is an open question left for future research. Its outcome decides whether reduction of IP_3 degradation offers new ways of addressing ataxia pharmacologically.

SUPPORTING MATERIAL

Supporting material can be found online at https://doi.org/10.1016/j.bpj.2021.03.027.

AUTHOR CONTRIBUTIONS

G.A. and F.M.S.d.S. designed research. V.N.F. performed research, contributed analytic tools. M.F. supervised simulations. V.N.F., M.F., and F.M.S.d.S. analyzed data and wrote the manuscript.

ACKNOWLEDGMENTS

This manuscript was developed within the scope of the IRTG 1740/TRP 2015/50122-0 and IRTG 1740/TRP2011/50151-0, funded by the DFG/FAPESP, and the DFG grant FA 350/13-1 to M.F. and FAPESP grant 2018/06504-4 to F.M.S.d.S.

SUPPORTING CITATIONS

References (91–97) appear in the Supporting material.

REFERENCES

1. Ito, M. 2002. The molecular organization of cerebellar long-term depression. *Nat. Rev. Neurosci.* 3:896–902.
2. Rose, C. R., and A. Konnerth. 2001. Stores not just for storage. intracellular calcium release and synaptic plasticity. *Neuron.* 31:519–522.
3. Daniel, H., C. Levenes, and F. Crépel. 1998. Cellular mechanisms of cerebellar LTD. *Trends Neurosci.* 21:401–407.
4. Kim, J. J., and R. F. Thompson. 1997. Cerebellar circuits and synaptic mechanisms involved in classical eyeblink conditioning. *Trends Neurosci.* 20:177–181.
5. Fiala, J. C., S. Grossberg, and D. Bullock. 1996. Metabotropic glutamate receptor activation in cerebellar Purkinje cells as substrate for adaptive timing of the classically conditioned eye-blink response. *J. Neurosci.* 16:3760–3774.

6. Finch, E. A., and G. J. Augustine. 1998. Local calcium signalling by inositol-1,4,5-trisphosphate in Purkinje cell dendrites. *Nature.* 396:753–756.
7. Takechi, H., J. Eilers, and A. Konnerth. 1998. A new class of synaptic response involving calcium release in dendritic spines. *Nature.* 396:757–760.
8. Piochon, C., H. K. Titley, …, C. Hansel. 2016. Calcium threshold shift enables frequency-independent control of plasticity by an instructive signal. *Proc. Natl. Acad. Sci. USA.* 113:13221–13226.
9. Coesmans, M., J. T. Weber, …, C. Hansel. 2004. Bidirectional parallel fiber plasticity in the cerebellum under climbing fiber control. *Neuron.* 44:691–700.
10. Tanaka, K., L. Khiroug, …, G. J. Augustine. 2007. Ca^{2+} requirements for cerebellar long-term synaptic depression: role for a postsynaptic leaky integrator. *Neuron.* 54:787–800.
11. Evans, R. C., and K. T. Blackwell. 2015. Calcium: amplitude, duration, or location? *Biol. Bull.* 228:75–83.
12. Jędrzejewska-Szmek, J., S. Damodaran, …, K. T. Blackwell. 2017. Calcium dynamics predict direction of synaptic plasticity in striatal spiny projection neurons. *Eur. J. Neurosci.* 45:1044–1056.
13. Kotaleski, J. H., and K. T. Blackwell. 2010. Modelling the molecular mechanisms of synaptic plasticity using systems biology approaches. *Nat. Rev. Neurosci.* 11:239–251.
14. Bhalla, U. S. 2004. Signaling in small subcellular volumes. I. Stochastic and diffusion effects on individual pathways. *Biophys. J.* 87:733–744.
15. Bhalla, U. S. 2004. Signaling in small subcellular volumes. II. Stochastic and diffusion effects on synaptic network properties. *Biophys. J.* 87:745–753.
16. Antunes, G., and F. M. Simoes de Souza. 2020. 3D modeling of dendritic spines with synaptic plasticity. *J. Vis. Exp* e60896.
17. Kitamura, K., and M. Kano. 2013. Dendritic calcium signaling in cerebellar Purkinje cell. *Neural Netw.* 47:11–17.
18. Nimchinsky, E. A., B. L. Sabatini, and K. Svoboda. 2002. Structure and function of dendritic spines. *Annu. Rev. Physiol.* 64:313–353.
19. Gipson, C. D., and M. F. Olive. 2017. Structural and functional plasticity of dendritic spines - root or result of behavior? *Genes Brain Behav.* 16:101–117.
20. Marr, D. 1969. A theory of cerebellar cortex. *J. Physiol.* 202:437–470.
21. Albus, J. S. 1971. A theory of cerebellar function. *Math. Biosci.* 10:25–61.
22. Yang, G., F. Pan, and W.-B. Gan. 2009. Stably maintained dendritic spines are associated with lifelong memories. *Nature.* 462:920–924.
23. Ito, M. 1989. Long-term depression. *Annu. Rev. Neurosci.* 12:85–102.
24. Augustine, G. J., F. Santamaria, and K. Tanaka. 2003. Local calcium signaling in neurons. *Neuron.* 40:331–346.
25. Eilers, J., G. J. Augustine, and A. Konnerth. 1995. Subthreshold synaptic Ca^{2+} signalling in fine dendrites and spines of cerebellar Purkinje neurons. *Nature.* 373:155–158.
26. Hartell, N. A. 1996. Strong activation of parallel fibers produces localized calcium transients and a form of LTD that spreads to distant synapses. *Neuron.* 16:601–610.
27. Miyakawa, H., V. Lev-Ram, …, W. N. Ross. 1992. Calcium transients evoked by climbing fiber and parallel fiber synaptic inputs in guinea pig cerebellar Purkinje neurons. *J. Neurophysiol.* 68:1178–1189.
28. Konnerth, A., J. Dreessen, and G. J. Augustine. 1992. Brief dendritic calcium signals initiate long-lasting synaptic depression in cerebellar Purkinje cells. *Proc. Natl. Acad. Sci. USA.* 89:7051–7055.
29. Bhalla, U. S., and R. Iyengar. 1999. Emergent properties of networks of biological signaling pathways. *Science.* 283:381–387.
30. Jiang, H., D. Wu, and M. I. Simon. 1994. Activation of phospholipase C beta 4 by heterotrimeric GTP-binding proteins. *J. Biol. Chem.* 269:7593–7596.
31. Sugiyama, T., M. Hirono, …, T. Yoshioka. 1999. Localization of phospholipase Cbeta isozymes in the mouse cerebellum. *Biochem. Biophys. Res. Commun.* 265:473–478.
32. Tanaka, J., S. Nakagawa, …, M. Watanabe. 2000. Gq protein alpha subunits Galphaq and Galpha11 are localized at postsynaptic extra-junctional membrane of cerebellar Purkinje cells and hippocampal pyramidal cells. *Eur. J. Neurosci.* 12:781–792.
33. Dupont, G., and C. Erneux. 1997. Simulations of the effects of inositol 1,4,5-trisphosphate 3-kinase and 5-phosphatase activities on Ca^{2+} oscillations. *Cell Calcium.* 22:321–331.
34. Irvine, R. F., and M. J. Schell. 2001. Back in the water: the return of the inositol phosphates. *Nat. Rev. Mol. Cell Biol.* 2:327–338.
35. Westenbroek, R. E., T. Sakurai, …, W. A. Catterall. 1995. Immunochemical identification and subcellular distribution of the alpha 1A subunits of brain calcium channels. *J. Neurosci.* 15:6403–6418.
36. Indriati, D. W., N. Kamasawa, …, R. Shigemoto. 2013. Quantitative localization of Cav2.1 (P/Q-type) voltage-dependent calcium channels in Purkinje cells: somatodendritic gradient and distinct somatic coclustering with calcium-activated potassium channels. *J. Neurosci.* 33:3668–3678.
37. Bagnall, M., S. du Lac, and M. Mauk. 2013. Chapter 31 - Cerebellum. *In* Fundamental Neuroscience, Fourth Edition. L. R. Squire, D. Berg, F. E. Bloom, S. du Lac, A. Ghosh, and N. C. Spitzer, eds. Academic Press, pp. 677–696.
38. Otis, T. S., P. J. Mathews, …, J. Maiz. 2012. How do climbing fibers teach? *Front. Neural Circuits.* 6:95.
39. Ito, M. 1970. Neurophysiological aspects of the cerebellar motor control system. *Int. J. Neurol.* 7:162–176.
40. Bastianelli, E. 2003. Distribution of calcium-binding proteins in the cerebellum. *Cerebellum.* 2:242–262.
41. Tolosa de Talamoni, N., C. A. Smith, …, J. T. Penniston. 1993. Immunocytochemical localization of the plasma membrane calcium pump, calbindin-D28k, and parvalbumin in Purkinje cells of avian and mammalian cerebellum. *Proc. Natl. Acad. Sci. USA.* 90:11949–11953.
42. Schmidt, H., K. M. Stiefel, …, J. Eilers. 2003. Mutational analysis of dendritic Ca^{2+} kinetics in rodent Purkinje cells: role of parvalbumin and calbindin D28k. *J. Physiol.* 551:13–32.
43. Schmidt, H., and J. Eilers. 2009. Spine neck geometry determines spino-dendritic cross-talk in the presence of mobile endogenous calcium binding proteins. *J. Comput. Neurosci.* 27:229–243.
44. Maeda, H., G. C. Ellis-Davies, …, H. Kasai. 1999. Supralinear Ca^{2+} signaling by cooperative and mobile Ca2+ buffering in Purkinje neurons. *Neuron.* 24:989–1002.
45. Antunes, G., A. C. Roque, and F. M. Simoes-de-Souza. 2018. Molecular mechanisms of detection and discrimination of dynamic signals. *Sci. Rep.* 8:2480.
46. Airaksinen, M. S., J. Eilers, …, M. Meyer. 1997. Ataxia and altered dendritic calcium signaling in mice carrying a targeted null mutation of the calbindin D28k gene. *Proc. Natl. Acad. Sci. USA.* 94:1488–1493.
47. Tada, M., M. Nishizawa, and O. Onodera. 2016. Roles of inositol 1,4,5-trisphosphate receptors in spinocerebellar ataxias. *Neurochem. Int.* 94:1–8.
48. Egorova, P. A., and I. B. Bezprozvanny. 2018. Inositol 1,4,5-trisphosphate receptors and neurodegenerative disorders. *FEBS J.* 285:3547–3565.
49. Foskett, J. K. 2010. Inositol trisphosphate receptor Ca^{2+} release channels in neurological diseases. *Pflugers Arch.* 460:481–494.
50. Ando, H., M. Hirose, and K. Mikoshiba. 2018. Aberrant IP_3 receptor activities revealed by comprehensive analysis of pathological mutations causing spinocerebellar ataxia 29. *Proc. Natl. Acad. Sci. USA.* 115:12259–12264.
51. Klockgether, T. 2010. Sporadic ataxia with adult onset: classification and diagnostic criteria. *Lancet Neurol.* 9:94–104.
52. Ramirez-Zamora, A., W. Zeigler, …, J. Biller. 2015. Treatable causes of cerebellar ataxia. *Mov. Disord.* 30:614–623.
53. Weng, G., U. S. Bhalla, and R. Iyengar. 1999. Complexity in biological signaling systems. *Science.* 284:92–96.
54. Kerr, R. A., T. M. Bartol, …, J. R. Stiles. 2008. Fast Monte Carlo simulation methods for biological reaction-diffusion systems in solution and on surfaces. *SIAM J. Sci. Comput.* 30:3126.

Please cite this article in press as: Friedhoff et al., Stochastic reaction-diffusion modeling of calcium dynamics in 3D dendritic spines of Purkinje cells, Biophysical Journal (2021), https://doi.org/10.1016/j.bpj.2021.03.027

55. Stiles, J. R., D. Van Helden, …, M. M. Salpeter. 1996. Miniature endplate current rise times less than 100 microseconds from improved dual recordings can be modeled with passive acetylcholine diffusion from a synaptic vesicle. *Proc. Natl. Acad. Sci. USA.* 93:5747–5752.

56. Stiles, J., and T. Bartol. 2001. Monte Carlo methods for simulating realistic synaptic microphysiology using MCell. *In* Computational Neuroscience: Realistic Modeling for Experimentalists. E. De Schutter, ed. CRC Press, pp. 87–127.

57. Hoops, S., S. Sahle, …, U. Kummer. 2006. COPASI–a COmplex PAthway SImulator. *Bioinformatics.* 22:3067–3074.

58. Franks, K. M., and T. J. Sejnowski. 2002. Complexity of calcium signaling in synaptic spines. *BioEssays.* 24:1130–1144.

59. Harris, K. M., and J. K. Stevens. 1988. Dendritic spines of rat cerebellar Purkinje cells: serial electron microscopy with reference to their biophysical characteristics. *J. Neurosci.* 8:4455–4469.

60. Bezprozvanny, I., and B. E. Ehrlich. 1994. Inositol (1,4,5)-trisphosphate (InsP3)-gated Ca channels from cerebellum: conduction properties for divalent cations and regulation by intraluminal calcium. *J. Gen. Physiol.* 104:821–856.

61. Okubo, Y., J. Suzuki, …, M. Iino. 2015. Visualization of Ca^{2+} filling mechanisms upon synaptic inputs in the endoplasmic reticulum of cerebellar Purkinje cells. *J. Neurosci.* 35:15837–15846.

62. Wang, S. S., W. Denk, and M. Häusser. 2000. Coincidence detection in single dendritic spines mediated by calcium release. *Nat. Neurosci.* 3:1266–1273.

63. Doi, T., S. Kuroda, …, M. Kawato. 2005. Inositol 1,4,5-trisphosphate-dependent Ca^{2+} threshold dynamics detect spike timing in cerebellar Purkinje cells. *J. Neurosci.* 25:950–961.

64. Antunes, G., A. C. Roque, and F. M. Simoes-de-Souza. 2016. Stochastic induction of long-term potentiation and long-term depression. *Sci. Rep.* 6:30899.

65. Xu, T., M. Naraghi, …, E. Neher. 1997. Kinetic studies of Ca^{2+} binding and Ca^{2+} clearance in the cytosol of adrenal chromaffin cells. *Biophys. J.* 73:532–545.

66. Antunes, G., A. M. Sebastião, and F. M. Simoes de Souza. 2014. Mechanisms of regulation of olfactory transduction and adaptation in the olfactory cilium. *PLoS One.* 9:e105531.

67. Lee, S. H., B. Schwaller, and E. Neher. 2000. Kinetics of Ca^{2+} binding to parvalbumin in bovine chromaffin cells: implications for $[Ca^{2+}]$ transients of neuronal dendrites. *J. Physiol.* 525:419–432.

68. Nägerl, U. V., D. Novo, …, J. L. Vergara. 2000. Binding kinetics of calbindin-D(28k) determined by flash photolysis of caged Ca^{2+}. *Biophys. J.* 79:3009–3018.

69. Takei, K., H. Stukenbrok, …, P. De Camilli. 1992. Ca2+ stores in Purkinje neurons: endoplasmic reticulum subcompartments demonstrated by the heterogeneous distribution of the InsP3 receptor, Ca^{2+}-ATPase, and calsequestrin. *J. Neurosci.* 12:489–505.

70. Falcke, M. 2004. Reading the patterns in living cells - the Physics of Ca^{2+} signaling. *Adv. Phys.* 53:255–440.

71. Sneyd, J., M. Falcke, …, C. Fox. 2004. A comparison of three models of the inositol trisphosphate receptor. *Prog. Biophys. Mol. Biol.* 85:121–140.

72. Dupont, G., M. Falcke, …, J. Sneyd. 2016. Models of Calcium Signalling, Volume 43 of Interdisciplinary Applied Mathematics. Springer, Cham, Switzerland.

73. Dupont, G., and J. Sneyd. 2017. Recent developments in models of calcium signalling. *Curr. Opin. Syst. Biol.* 3:15–22.

74. Moraru, I. I., E. J. Kaftan, …, J. Watras. 1999. Regulation of type 1 inositol 1,4,5-trisphosphate-gated calcium channels by InsP3 and calcium: simulation of single channel kinetics based on ligand binding and electrophysiological analysis. *J. Gen. Physiol.* 113:837–849.

75. Taylor, C. W., and V. Konieczny. 2016. IP_3 receptors: take four IP_3 to open. *Sci. Signal.* 9:pe1.

76. De Young, G. W., and J. Keizer. 1992. A single-pool inositol 1,4,5-trisphosphate-receptor-based model for agonist-stimulated oscillations in Ca^{2+} concentration. *Proc. Natl. Acad. Sci. USA.* 89:9895–9899.

77. Khodakhah, K., and D. Ogden. 1993. Functional heterogeneity of calcium release by inositol trisphosphate in single Purkinje neurones, cultured cerebellar astrocytes, and peripheral tissues. *Proc. Natl. Acad. Sci. USA.* 90:4976–4980.

78. Kotaleski, J. H., D. Lester, and K. T. Blackwell. 2002. Subcellular interactions between parallel fibre and climbing fibre signals in Purkinje cells predict sensitivity of classical conditioning to interstimulus interval. *Integr. Physiol. Behav. Sci.* 37:265–292.

79. Thul, R., and M. Falcke. 2004. Release currents of IP_3 receptor channel clusters and concentration profiles. *Biophys. J.* 86:2660–2673.

80. Bentele, K., and M. Falcke. 2007. Quasi-steady approximation for ion channel currents. *Biophys. J.* 93:2597–2608.

81. Koumura, T., H. Urakubo, …, S. Kuroda. 2014. Stochasticity in Ca^{2+} increase in spines enables robust and sensitive information coding. *PLoS One.* 9:e99040.

82. Fujii, M., K. Ohashi, …, S. Kuroda. 2017. Small-volume effect enables robust, sensitive, and efficient information transfer in the spine. *Biophys. J.* 112:813–826.

83. Bell, M., T. Bartol, …, P. Rangamani. 2019. Dendritic spine geometry and spine apparatus organization govern the spatiotemporal dynamics of calcium. *J. Gen. Physiol.* 151:1017–1034.

84. Han, V. Z., Y. Zhang, …, C. Hansel. 2007. Synaptic plasticity and calcium signaling in Purkinje cells of the central cerebellar lobes of mormyrid fish. *J. Neurosci.* 27:13499–13512.

85. Ke, M. C., C. C. Guo, and J. L. Raymond. 2009. Elimination of climbing fiber instructive signals during motor learning. *Nat. Neurosci.* 12:1171–1179.

86. Gaffield, M. A., A. Bonnan, and J. M. Christie. 2019. Conversion of graded presynaptic climbing fiber activity into graded postsynaptic Ca^{2+} signals by Purkinje cell dendrites. *Neuron.* 102:762–769.e4.

87. Roh, S.-E., S. H. Kim, …, S. J. Kim. 2020. Direct translation of climbing fiber burst-mediated sensory coding into post-synaptic Purkinje cell dendritic calcium. *eLife.* 9:e61593.

88. Ait Ouares, K., and M. Canepari. 2020. The origin of physiological local mGluR1 supralinear Ca^{2+} signals in cerebellar Purkinje neurons. *J. Neurosci.* 40:1795–1809.

89. Thurley, K., I. F. Smith, …, M. Falcke. 2011. Timescales of IP_3-evoked Ca^{2+} spikes emerge from Ca^{2+} puffs only at the cellular level. *Biophys. J.* 101:2638–2644.

90. Cao, P., G. Donovan, …, J. Sneyd. 2013. A stochastic model of calcium puffs based on single-channel data. *Biophys. J.* 105:1133–1142.

91. Blackwell, K. T. 2013. Approaches and tools for modeling signaling pathways and calcium dynamics in neurons. *J. Neurosci. Methods.* 220:131–140.

92. Blender Online Community. 2019. Blender - a 3D modelling and rendering package. Blender Foundation, https://www.blender.org/.

93. Stauffer, T. P., D. Guerini, and E. Carafoli. 1995. Tissue distribution of the four gene products of the plasma membrane Ca^{2+} pump. A study using specific antibodies. *J. Biol. Chem.* 270:12184–12190.

94. Lytton, J., M. Westlin, …, D. H. MacLennan. 1992. Functional comparisons between isoforms of the sarcoplasmic or endoplasmic reticulum family of calcium pumps. *J. Biol. Chem.* 267:14483–14489.

95. Allbritton, N. L., T. Meyer, and L. Stryer. 1992. Range of messenger action of calcium ion and inositol 1,4,5-trisphosphate. *Science.* 258:1812–1815.

96. Dickinson, G. D., K. L. Ellefsen, …, I. Parker. 2016. Hindered cytoplasmic diffusion of inositol trisphosphate restricts its cellular range of action. *Sci. Signal.* 9:ra108.

97. Kakiuchi, S., S. Yasuda, …, K. Sobue. 1982. Quantitative determinations of calmodulin in the supernatant and particulate fractions of mammalian tissues. *J. Biochem.* 92:1041–1048.

Biophysical Journal, Volume *120*

Supplemental information

Stochastic reaction-diffusion modeling of calcium dynamics in 3D dendritic spines of Purkinje cells

Victor Nicolai Friedhoff, Gabriela Antunes, Martin Falcke, and Fabio M. Simões de Souza

Manuscript submitted to **Biophysical***Journal*
Article

Supporting Material to Stochastic reaction-diffusion modeling of calcium dynamics in 3D-dendritic spines of Purkinje Cells

Victor Nicolai Friedhoff[1,2], Gabriela Antunes[3], Martin Falcke[1,2], and Fabio M. Simões de Souza[3,a]

[1]Mathematical Cell Physiology, Max Delbrück Center for Molecular Medicine, Berlin, Germany
[2]Department of Physics, Humboldt University, Berlin, Germany
[3]Center for Mathematics, Computation, and Cognition, Federal University of ABC, São Bernardo do Campo, SP, Brasil
[a]Correspondence: fabio.souza@ufabc.edu.br

1 SUPPORTING MATERIAL

1.1 Simulation methods

We constructed the three-dimensional geometry of a dendritic spine in Blender, a free open-source software used to create three-dimensional geometries (1). We then used CellBlender to incorporate the dendrite's geometry with the biophysical model and MCell 3.4 (2–4) to run stochastic simulations. MCell is a stochastic single particle simulator of reaction-diffusion systems in three dimensions. All particles are tracked over variable time steps and diffuse by a discrete random walk through a predefined volume using ray-tracing techniques. The length of each spatial step during the random walk is determined by the diffusion constant of the particle species and the current time step. Particles can be set to diffuse on predefined surfaces or in volumes. Reactions of particle species can be specified by first- and second-order reaction kinetics, resp. Ray-marching is used to propagate rays after collisions and Monte Carlo probabilities are used to decide about triggering reactions. When two particles are close enough, MCell determines the reaction probabilities in dependence on the specific reaction rates, a set of predefined random numbers ('seeds'), and time step which then leads to stochastic reaction events.

The positions of all particles, including IP_3R, SERCA, and leak channel molecules on the ER membrane and PMCA, NCX, and leak channel molecules on the spine membrane depend on the used seed, i.e. are randomly chosen individually for each simulation run.

In parallel, we modeled the system's Ca^{2+} response in terms of coupled ordinary differential equations (ODEs) describing average particle concentrations using Copasi (5). While MCell offers a biophysically realistic approach to a biological problem, accounting for low particle concentrations, inherent stochasticity and complex three-dimensional geometries (6), Copasi describes the kinetic reactions in a well-mixed volume efficiently, without the influence of diffusion or complex geometry. In this way, the dynamics of the model can be tested in a computationally fast environment before going into more expensive reaction-diffusion simulations in complex geometries. Copasi was for instance used to approximately find concentrations of each species at equilibrium, i.e. the initial state. An overview over different deterministic and stochastic simulation tools used in computation biology can be found in (7).

We chose one spatial compartment with the same volume as in MCell with $V_{compartment} = 0.512\ \mu m^3$ in Copasi to have an agreeing notion of concentrations and particle numbers, but did not account for any kind of complex geometry. Dynamics were modeled in terms of spatially homogeneous deterministic concentrations of particle species, described by a set of coupled ODEs in contrast to stochastic interactions of single particles diffusing in a complex volume in MCell.

1.2 IP_3R Receptor models

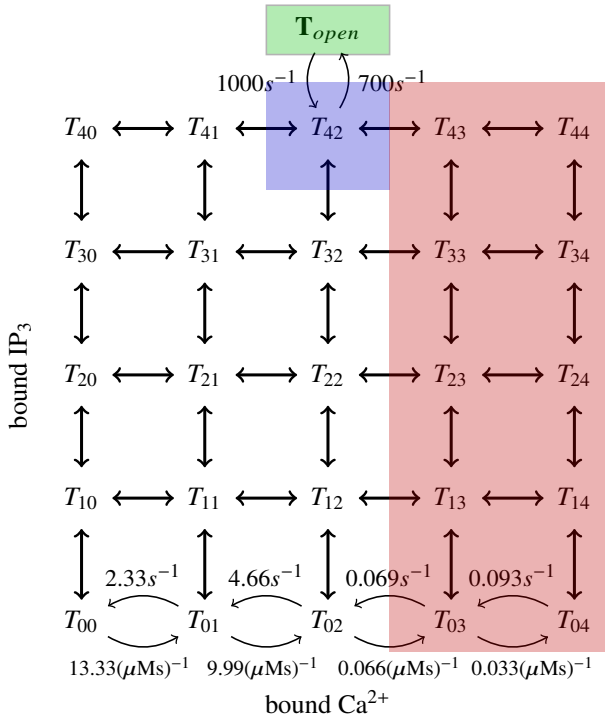

Figure S1: Extended visualisation of Moraru's IP_3R model.

(left) Subsection of Moraru's IP_3R model with example rates shown for binding and unbinding of Ca^{2+} and transition in to and from open state T_{open}. When four IP_3 and two Ca^{2+} (activating) are bound, T_{42} (blue), there is a probability to go into the open state T_{open} (green), whence additional Ca^{2+} will be released. Further Ca^{2+} binding of the IP_3R will lower the probability of opening, effectively promoting the ten states T_{x3} and T_{x4} to inhibitory Ca^{2+} states (red), $x \in [0, 4]$.

(right) Table of parameters used for Moraru's IP_3R model. The reaction rates of binding Ca^{2+} or IP_3 are proportional to the available binding sites, while dissociation rates are proportional to the number of bound Ca^{2+} or IP_3. We get e.g. $T_{4x} \rightarrow T_{3x} + IP_3$ with $k = 4 \cdot k_{IP3\text{-}Off} = 4 \cdot 25s^{-1} = 100s^{-1}$ because there are 4 independently bound IP_3 that can trigger the decay into state T_{3x}. Additionally, we set the Ca^{2+} binding and dissociation rates of the inhibitory states to be slower than into or from the activating states, expressed by the scaling ratio r_s. We get e.g. $T_{x2} + Ca^{2+} \rightarrow T_{x3}$ with $k = 2 \cdot r_s \cdot k_{CaOn} = 2 \cdot 0.01 \cdot 3.3\ (\mu Ms)^{-1} = 0.066\ (\mu Ms)^{-1}$.

Moraru's IP_3R model

reactions		on rate	off rate
	excitatory		
$T_{x0} + Ca^{2+}$	$\leftrightarrow T_{x1}$	13.33 $(\mu M\ s)^{-1}$	2.33 s^{-1}
$T_{x1} + Ca^{2+}$	$\leftrightarrow T_{x2}$	9.99 $(\mu M\ s)^{-1}$	4.66 s^{-1}
	inhibitory	(here r_s=0.01)	
$T_{x2} + Ca^{2+}$	$\leftrightarrow T_{x3}$	0.066 $(\mu M\ s)^{-1}$	0.069 s^{-1}
$T_{x3} + Ca^{2+}$	$\leftrightarrow T_{x4}$	0.033 $(\mu M\ s)^{-1}$	0.093 s^{-1}
	IP_3		
$T_{0x} + IP_3$	$\leftrightarrow T_{1x}$	333.33 $(\mu M\ s)^{-1}$	25 s^{-1}
$T_{1x} + IP_3$	$\leftrightarrow T_{2x}$	249.99 $(\mu M\ s)^{-1}$	50 s^{-1}
$T_{2x} + IP_3$	$\leftrightarrow T_{3x}$	166.66 $(\mu M\ s)^{-1}$	75 s^{-1}
$T_{3x} + IP_3$	$\leftrightarrow T_{4x}$	83.33 $(\mu M\ s)^{-1}$	100 s^{-1}
	opening		
T_{42}	$\leftrightarrow T_{open}$	700 s^{-1}	1000 s^{-1}
T_{open}	$\rightarrow Ca^{2+}$ release	10000 s^{-1}	

Table S1: Table with parameter values used for Moraru's IP_3R model (8).

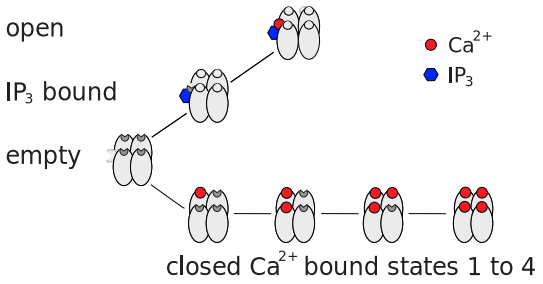

Figure S2: Extended visualisation of Doi's IP_3R model

Doi's IP_3R model

reactions		on rate	off rate
$IP3R_o$	$\rightarrow Ca^{2+}$ release	5400 s^{-1}	
$IP3R_i + Ca^{2+}$	$\leftrightarrow IP3R_o$	8000 $(\mu M\ s)^{-1}$	2000 s^{-1}
$IP3R + IP_3$	$\leftrightarrow IP3R_i$	1000 $(\mu M\ s)^{-1}$	25800 s^{-1}
$IP3R + Ca^{2+}$	$\leftrightarrow IP3R_{c1}$	8.88 $(\mu M\ s)^{-1}$	5 s^{-1}
$IP3R_{c1} + Ca^{2+}$	$\leftrightarrow IP3R_{c2}$	19.98 $(\mu M\ s)^{-1}$	10 s^{-1}
$IP3R_{c2} + Ca^{2+}$	$\leftrightarrow IP3R_{c3}$	39.96 $(\mu M\ s)^{-1}$	15 s^{-1}
$IP3R_{c3} + Ca^{2+}$	$\leftrightarrow IP3R_{c4}$	59.94 $(\mu M\ s)^{-1}$	20 s^{-1}

Table S2: Reaction rates used for Doi's IP_3R model (9).

(left) IP_3R model from Doi et al. (9). The IP_3Racts as an coincidence detector and only opens if IP_3 attaches before Calcium does. Otherwise it acts as an buffer and goes into the closed states. **(right)** Reaction rates used for Doi's IP_3R model.

1.3 Reaction rates

1.3.1 Buffer rates

Buffer reactions		on rate	off rate	source
Ca^{2+} + Pv	↔ CaPv	107 (μM s)$^{-1}$	0.95 s^{-1}	(10)
Pv	↔ PvMg	472 s^{-1}	25.0 s^{-1}	
Ca^{2+} + Cb	↔ CbCa1	43.5 (μM s)$^{-1}$	35.8 s^{-1}	(11)
CbCa1 + Ca^{2+}	↔ CbCa2	5.5 (μM s)$^{-1}$	2.60 s^{-1}	
Ca^{2+} + CaM	↔ CaM1000	750 (μM s)$^{-1}$	50000 s^{-1}	(12)
Ca^{2+} + CaM	↔ CaM0100	750 (μM s)$^{-1}$	50000 s^{-1}	
Ca^{2+} + CaM	↔ CaM0010	800 (μM s)$^{-1}$	20000 s^{-1}	
Ca^{2+} + CaM	↔ CaM0001	204.6 (μM s)$^{-1}$	5115 s^{-1}	
CaM1000 + Ca^{2+}	↔ CaM1100	750 (μM s)$^{-1}$	625 s^{-1}	
CaM0100 + Ca^{2+}	↔ CaM1100	750 (μM s)$^{-1}$	625 s^{-1}	
CaM0010 + Ca^{2+}	↔ CaM0011	204.6 (μM s)$^{-1}$	25.575 s^{-1}	
CaM0001 + Ca^{2+}	↔ CaM0011	800 (μM s)$^{-1}$	100 s^{-1}	
CaM1000 + Ca^{2+}	↔ CaM1010	800 (μM s)$^{-1}$	20000 s^{-1}	
CaM1000 + Ca^{2+}	↔ CaM1001	204.6 (μM s)$^{-1}$	5115 s^{-1}	
CaM0100 + Ca^{2+}	↔ CaM0110	800 (μM s)$^{-1}$	20000 s^{-1}	
CaM0100 + Ca^{2+}	↔ CaM0101	204.6 (μM s)$^{-1}$	5115 s^{-1}	
CaM0010 + Ca^{2+}	↔ CaM1010	750 (μM s)$^{-1}$	50000 s^{-1}	
CaM0010 + Ca^{2+}	↔ CaM0110	750 (μM s)$^{-1}$	50000 s^{-1}	
CaM0001 + Ca^{2+}	↔ CaM1001	750 (μM s)$^{-1}$	50000 s^{-1}	
CaM0001 + Ca^{2+}	↔ CaM0101	750 (μM s)$^{-1}$	50000 s^{-1}	
CaM1100 + Ca^{2+}	↔ CaM1110	800 (μM s)$^{-1}$	20000 s^{-1}	
CaM1100 + Ca^{2+}	↔ CaM1101	204.6 (μM s)$^{-1}$	5115 s^{-1}	
CaM0011 + Ca^{2+}	↔ CaM1011	750 (μM s)$^{-1}$	50000 s^{-1}	
CaM0011 + Ca^{2+}	↔ CaM0111	750 (μM s)$^{-1}$	50000 s^{-1}	
CaM1010 + Ca^{2+}	↔ CaM1110	750 (μM s)$^{-1}$	625 s^{-1}	
CaM0110 + Ca^{2+}	↔ CaM1110	750 (μM s)$^{-1}$	625 s^{-1}	
CaM1001 + Ca^{2+}	↔ CaM1101	750 (μM s)$^{-1}$	625 s^{-1}	
CaM0101 + Ca^{2+}	↔ CaM1101	750 (μM s)$^{-1}$	625 s^{-1}	
CaM1010 + Ca^{2+}	↔ CaM1011	204.6 (μM s)$^{-1}$	25.575 s^{-1}	
CaM0110 + Ca^{2+}	↔ CaM0111	204.6 (μM s)$^{-1}$	25.575 s^{-1}	
CaM1001 + Ca^{2+}	↔ CaM1011	800 (μM s)$^{-1}$	100 s^{-1}	
CaM0101 + Ca^{2+}	↔ CaM0111	800 (μM s)$^{-1}$	100 s^{-1}	
CaM1110 + Ca^{2+}	↔ CaM1111	204.6 (μM s)$^{-1}$	25.575 s^{-1}	
CaM1101 + Ca^{2+}	↔ CaM1111	800 (μM s)$^{-1}$	100 s^{-1}	
CaM1011 + Ca^{2+}	↔ CaM1111	750 (μM s)$^{-1}$	625 s^{-1}	
CaM0111 + Ca^{2+}	↔ CaM1111	750 (μM s)$^{-1}$	625 s^{-1}	

Table S3: Rates used for buffer reactions. Rates of Fluo-5F were chosen according to their K_d and concentrations (13).

1.3.2 Ca^{2+} transporter and IP_3 reaction rates

Reaction		on rate	off rate	source
PMCA + Ca^{2+}	$\leftrightarrow$ PMCA1	2500 $(\mu M\ s)^{-1}$	2000 s^{-1}	(12, 14)
PMCA1	$\rightarrow$ PMCA	125 s^{-1}		(12)
SERCA + Ca^{2+}	$\leftrightarrow$ SERCA1	17147 $(\mu M\ s)^{-1}$	8426.3 s^{-1}	(12, 15)
SERCA1 + Ca^{2+}	$\leftrightarrow$ SERCA2	17147 $(\mu M\ s)^{-1}$	8426.3 s^{-1}	(12, 15)
SERCA2	$\rightarrow$ SERCA	250 s^{-1}		(16)
NCX + Ca^{2+}	$\leftrightarrow$ NCX1	800 $(\mu M\ s)^{-1}$	100 s^{-1}	(12)
NCX1	$\rightarrow$ NCX	2300 s^{-1}		(12)
Leak ER	Ca^{2+} release	26 s^{-1}		us
Leak Den	Ca^{2+} release	26 s^{-1}		us
$IP3_{caged}$	$\rightarrow$ IP3	7 s^{-1}		us
IP3	$\rightarrow$ NULL	15 s^{-1}		us

Table S4: Reaction rates for Ca^{2+} transporters and leaks, as well as rates for decay of caged IP_3 to IP_3 and degradation of IP_3.

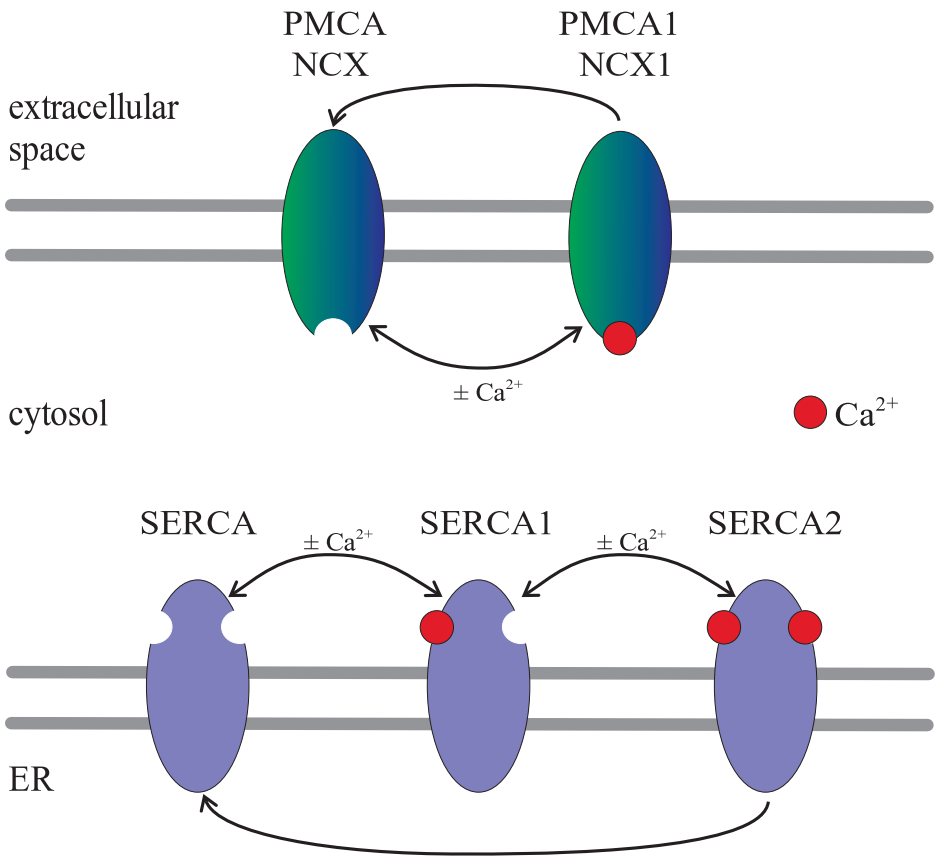

Figure S3: Graphical representation of SERCA, PMCA and NCX models used. Double-headed arrows indicate binding and unbinding of Ca^{2+}, while one-headed arrows indicate decay (removal of Ca^{2+}).

1.4 Geometry

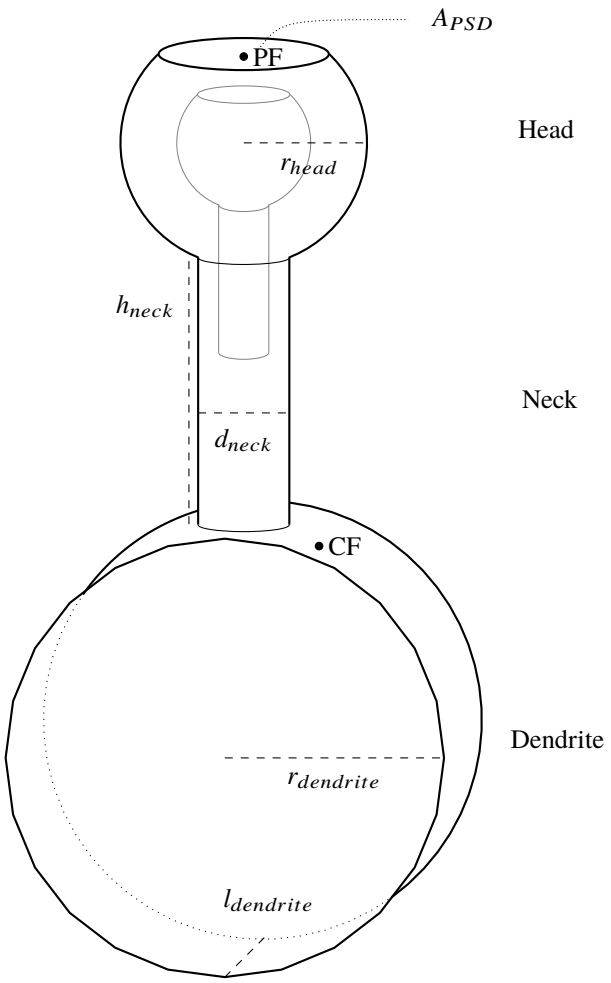

Spatial parameters

Segment		Volume in μm^3
Spine head	V_{head}	0.100
Spine neck	V_{neck}	0.021
Dendrite	$V_{dendrite}$	0.391
Total volume	V	0.512
ER head	$V_{ER,head}$	0.017
ER neck	$V_{ER,neck}$	0.003
ER volume	V_{ER}	0.020
Segment		Area in μm^2
PSD	A_{PSD}	0.152
ER surface	A_{ER}	0.445
Segment		Length in μm
PSD Radius	r_{PSD}	0.22
Spine head radius	r_{head}	0.30
Spine neck diameter	d_{neck}	0.20
Spine neck height	h_{neck}	0.58 to 0.60
ER head radius	$r_{ER,head}$	0.163
ER neck height	$r_{ER,neck}$	0.33
Dendrite radius	$r_{dendrite}$	0.50
Dendrite length	$l_{dendrite}$	0.50

Figure S4: Spatial parameters of geometry based on measurements from (17), created in Blender (1).

For the calculation of particle concentrations in the spine head we used the volume of the cytosolic part of the spine head, $V_{head,\,cytosol} \approx 0.082 \mu m^3$, therefore 50 particles $\approx 1\ \mu$M.

During Ca^{2+} transients, the spine head traps Ca^{2+} and thereby acts as a sink. While the concentration in the spine head is approximately constant, it decreases linearly along the length of the neck down the z-axis, until it is constant again in the dendrite element. An example of this is shown in Movie S5, where the geometry was cut into 200 slices along the z-axis and Ca^{2+} in these slices was plotted against the z-axis in the geometry.

1.5 Particle concentrations and diffusion coefficients

Molecule	concentration	# of molecules	source	diffusion coefficient	source
Calcium (Ca^{2+})	50nM	15	(18, 19)	223 $\mu m^2 s^{-1}$	(11, 20)
Inositol trisphosphate (IP_3)				10 $\mu m^2 s^{-1}$	(21)
caged IP_3		1400		280 $\mu m^2 s^{-1}$	us
Parvalbumin (PV)	40μM	11845	(19)	43 $\mu m^2 s^{-1}$	(11)
Calbindin (Cb)	40μM	11845	(19)	28 $\mu m^2 s^{-1}$	(11)
Calmodulin (CaM)	19μM	5625	(16, 22)	25 $\mu m^2 s^{-1}$ empty, 2.5 $\mu m^2 s^{-1}$ Ca^{2+} bound	
Magnesium (Mg^{2+})	590μM		(11)		
IP_3R Doi's model		60	estimated, (23)		
IP_3R Moraru's model		52, 54, 56	estimated, (23)		
SERCA		68	(16)		
PMCA		13	(16)		
NCX		5	(16)		
Dendrite Leak		10			
ER Leak		10			

Table S5: Total and basal concentrations, particle numbers, and diffusion coefficients of particle species. Mg^{2+} and Fluo-5F were not modeled explicitly, but only as part of pseudo first-order reactions. Ca^{2+} transporters were set to be unmovable. Caged IP_3 was confined to a small box volume in the PSD, only free IP_3 was allowed to leave that box.

Subspecies concentrations for the basal state s.t. $[Ca^{2+}_{free}] \approx 50$nM in equilibrium as determined in Copasi are

Species	Total #	Substates	#
Free Ca^{2+}	15		
PV	11845	PV	464
		PVCa	2619
		PVMg	8760
Cb	11845	Cb	11112
		CbCa1	677
		CbCa2	71
CaM	5625	CaM	5592
		CaM0001	11
		CaM0010	11
		CaM0100	4
		CaM1000	3
		CaM0011	4
SERCA	68	SERCA	61
		SERCA1	6
		SERCA2	1
PMCA	13	PMCA	12
		PMCA1	1
NCX	5	NCX	5

Table S6: Particle numbers of subspecies at steady state.

All other substates did not occur in the basal state.

1.6 Results - Doi's IP_3R model

1.6.1 MCell

See results section 3.1 on Doi's model and Fig. S5.

1.6.2 Copasi

We included Doi's IP_3R model (9), buffers and Ca^{2+} transporters into one compartment in Copasi and studied the Ca^{2+} transients in response to different Ca^{2+} amplitudes of the PF and CF stimuli for the cases of PF burst and PF burst + CF. We used up-to-date parameter values that differ from Doi et al. to agree with current literature and to be able to create Ca^{2+} transients of similar properties.

The peak of the Ca^{2+} transient weakly depends on the Ca^{2+} amplitude of the PF burst stimulus, Fig. S6, when no CF stimulus is present. Without changing $[IP_3](t)$ the peak value of the transient increases from about $p(PF = 0\mu M) = 1.6\mu M$ to saturating at $p(PF > 0.4\mu M) = 1.8\mu M$, an increase of about 12.5%.

When we choose one PF Ca^{2+} amplitude per spike of the PF burst, e.g. $PF = 0.25\mu M$, and add a CF stimulus, we can scale the peak of the resulting Ca^{2+} transient by changing the Ca^{2+} amplitude of the CF stimulus, Fig. S7. The transient shows no peak saturation for low to medium CF Ca^{2+} amplitudes. We can scale the peak from $p(CF = 0) = 1.8\mu M$ to e.g. $p(CF = 6\mu M) = 9\mu M$, Fig. S7, an increase of about 500%, way beyond the 150% required as estimated from experimental data (13).

1.7 Results - Moraru's IP_3R model

1.7.1 Copasi

We replaced Doi's IP_3R model by Moraru's IP_3R model, computed a new steady state, and subjected the system to the same PF and CF stimuli. We find that the system reacts much more sensitively to Ca^{2+} input coming from either PF or CF stimuli. For PF stimuli, there is no convergence of transients for low to intermediate PF Ca^{2+} amplitudes compared to Doi, Fig. S6. The maximal scaling also increases by about a factor of 5 for the stimuli chosen in Fig. S8, with the peak around $p(PF = 0) = 0.3\mu M$ to $p(PF = 0.3\mu M) = 1.6\mu M$. When adding a CF stimulus to the PF burst we can influence the resulting Ca^{2+} transient easily. Even for small values of CF Ca^{2+} amplitude (compared to the results with Doi's model, Fig. S7), we can increase the Ca^{2+} response massively from about 1.5 μM without CF stimulus to 9 μM with CF = 0.8 μM, Fig. S9.

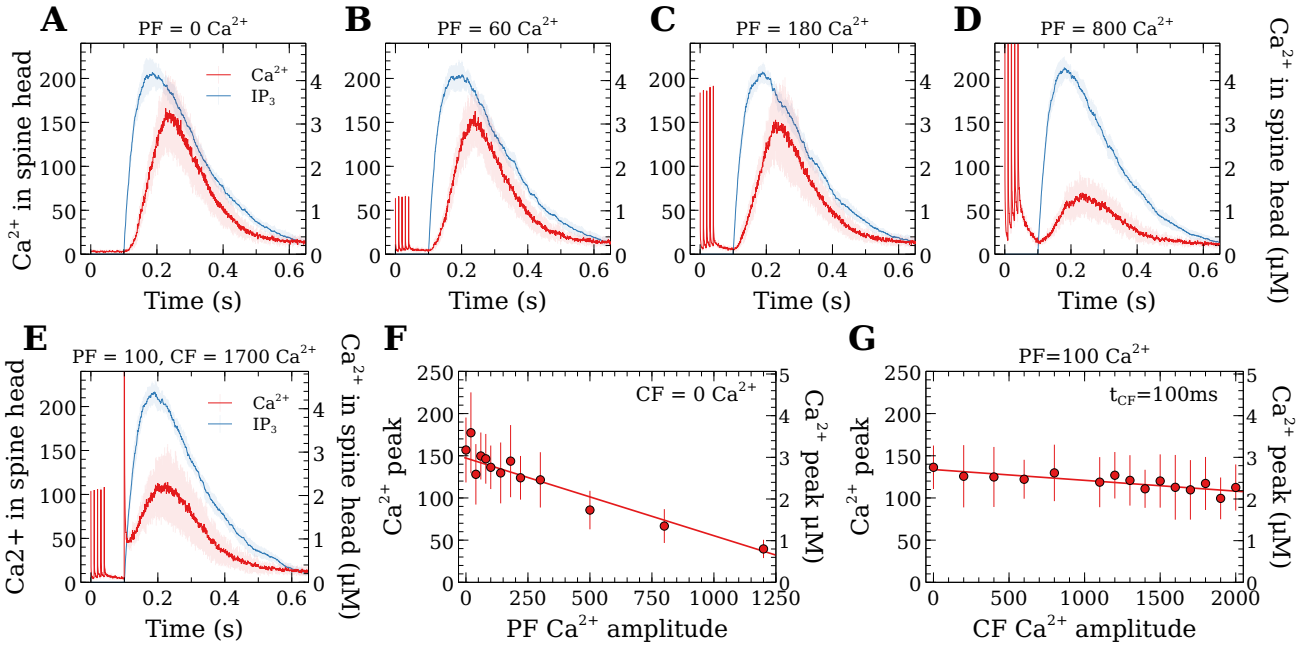

Figure S5: **(A-D)** IP_3R induced Ca^{2+} transients using Doi's IP_3R model in MCell in response to PF burst stimulus of variable Ca^{2+} amplitude a) PF=0 Ca^{2+}, b) PF=60 Ca^{2+}, c) PF=180 Ca^{2+}, d) PF=800 Ca^{2+}. Plots are averages (red Ca^{2+}, blue IP_3) and standard deviations (opaque areas) of 12 stochastic simulations. **(E)** Example IP_3R induced Ca^{2+} transient (red) from PF burst stimulus with CF coactivation at $t_{CF} = 100\ ms$ with PF=100 Ca^{2+} and CF=1700 Ca^{2+}, and IP_3 (blue). **(F)** Ca^{2+} transient peak values for a large range of PF Ca^{2+} amplitudes without CF coactivation. **(G)** Ca^{2+} transient peak values for a large range of CF Ca^{2+} amplitudes with $t_{CF} = 100\ ms$ for PF burst + CF stimulation. Parameters not explicitly mentioned are given in Table S2. Data points in (F) and (G) are averages of 12 simulations each, error bars indicate standard deviations.

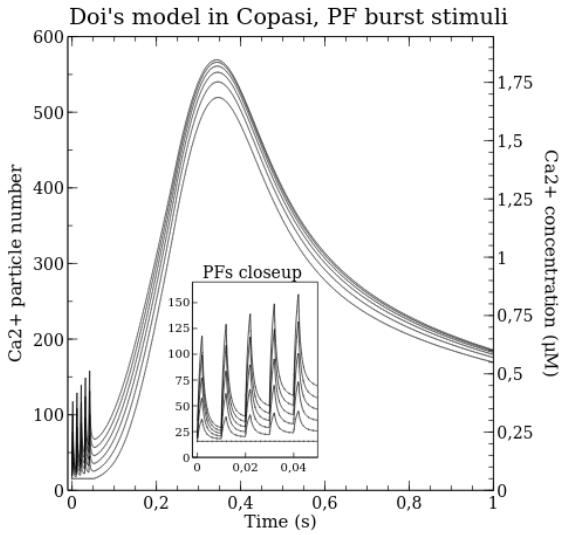

Figure S6: Doi's model, Ca^{2+} transients with different Ca^{2+} per PF spike, 0 (yielding the smallest Ca^{2+} transient) to approximately 0.4μM (yielding the largest Ca^{2+} transient). Increasing Ca^{2+} from PF spikes does increase the peak of the Ca^{2+} transient, but saturates at about 1.8μM. Closeup of PF spikes is visible in the smaller plot.

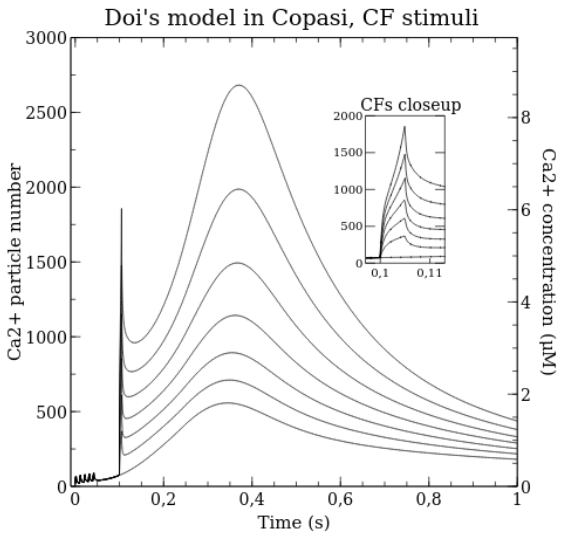

Figure S7: Doi's model, Ca^{2+} transient with different Ca^{2+} per CF stimulus and closeup of CF Ca^{2+} spikes. The peak of the Ca^{2+} transient depends strongly on the Ca^{2+} amplitude of the CF stimulus. We can scale the peak from $p(CF = 0) = 1.8\mu$M to e.g. $p(CF = 6\mu\text{M}) = 9\mu$M, an increase of about 500%.

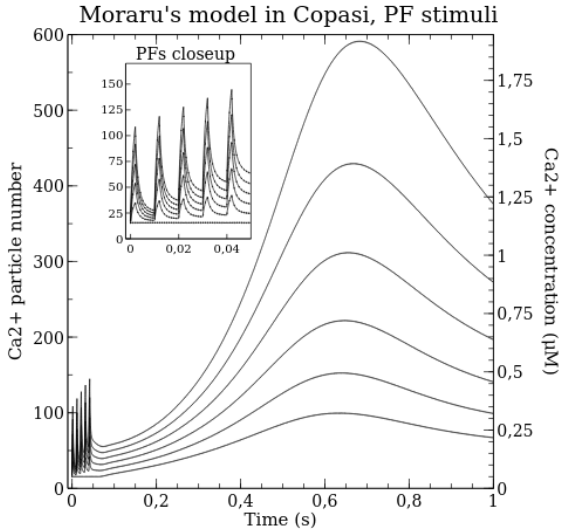

Figure S8: Moraru's model, Ca^{2+} transient with different Ca^{2+} per one PF stimulus, 0 to 0.4uM. Increasing PF Ca^{2+} amplitude clearly increases the peak of the Ca^{2+} transient. There is no saturation at low to intermediate PF Ca^{2+} amplitudes and the transient reacts more sensitively to PF stimuli, showing an peak increase of about 500% from no PF stimulus to an PF Ca^{2+} amplitude of about 0.4μM.

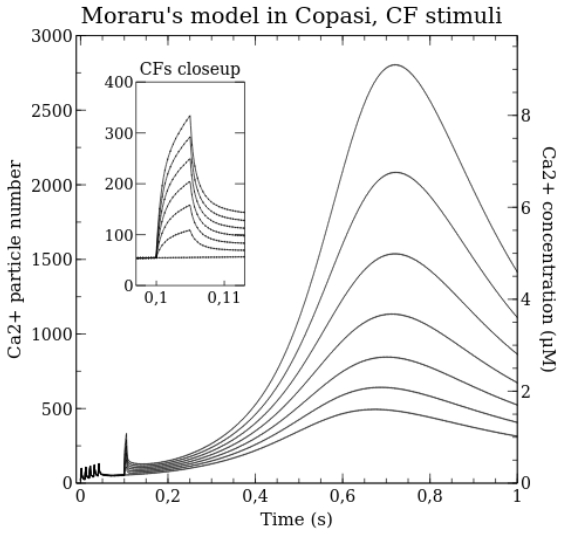

Figure S9: Moraru's model, Ca^{2+} transient for a chosen constant PF Ca^{2+} amplitude of PF=0.25 μM and variable CF Ca^{2+} amplitudes. In comparison to Doi's model, Moraru's model requires much smaller CF Ca^{2+} amplitudes to reach higher peak values of the resulting Ca^{2+} transient. An increase of the Ca^{2+} transient's peak value of 150% with CF coactivation following experimental data from Piochon et al (13) is easily archived.

1.7.2 Comparison to optimal time window data by Wang et al.

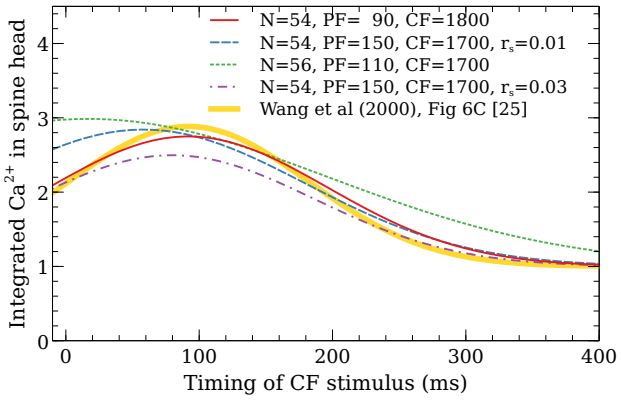

Figure S10: Integral from 0.1s to 0.8s of Ca^{2+} transients against timing of CF stimulus for the same data as in Fig. 8. We plot the Gaussian fits to the data points only. We compare them with the Gaussian which was fit to the experimental data by Wang et al. in (24). The blue (green) set is set B (C) in Fig. 6. A rather small change of parameter values (red) leads to good agreement with the experimental results from Wang et al. (24).

1.7.3 Buffers

Buffers modulate the amplitude of the free Ca^{2+} transient. We studied the Ca^{2+} peak amplitude modulation of the buffer species Pv, CaM, and Cb by removing them individually and ran simulations with a PF burst and a PF burst + CF stimulus.

Removing any buffer species led to an increase of the Ca^{2+} transient peak value with Pv having the weakest effect for both cases with and without CF coactivation. Its Ca^{2+} binding site (K_d = 8.8 nM) is occupied mainly by Mg^{2+} at the resting Ca^{2+} concentration of 50 nM. Ca^{2+} replaces Mg^{2+} (see Fig. S11A) with increasing concentration and is buffered that way by Pv. Therefore Pv becomes more relevant for higher [Ca^{2+}] only.

We find that Cb has the strongest effect on peak values, followed by CaM and then Pv, Fig. S11A. This is in agreement with buffer concentrations ([Cb]=40 μM, [CaM]=19 μM) and the dissociation constants K_d for the different Ca^{2+} binding sites of CaM (K_d = 0.125 μM to 66.6 μM) and Cb (K_d = 0.473 μM to 0.823 μM).

Additionally, our results show that buffers do not only influence Ca^{2+} transient peak values, but also positive and negative feedback of Ca^{2+} on IP_3Rs. Fig. S11B shows the average of the total number of released Ca^{2+}. Removing Cb has the strongest influence for a PF burst again and yields a very strong increase in IP_3R Ca^{2+} release. It almost reaches the release of the PF burst + CF coactivation scenario with all buffer species present. Once the CF stimulus has happened, the differences between the four scenarios is less prominent, but removing Cb still increases IP_3R activity the most.

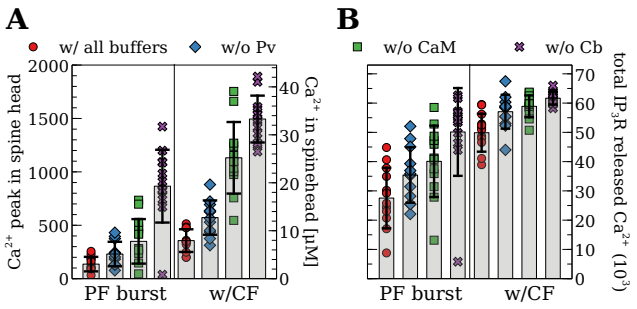

Figure S11: **(A)** Peaks of Ca^{2+} transients from simulations with different buffer contents. Full circles (red) are peak values of Ca^{2+} transients with all three buffer species included, while the rest show peak values for cases with either Pv, CaM, or Cb removed. **(B)** Total number of Ca^{2+} released from IP_3Rs with either all buffers included or one buffer species removed, same color and symbol scheme as in A. Individual symbols show the 12 simulations which were used to calculate averages and standard deviations, shown as bars.

1.7.4 Single PF stimulus with CF coactivation

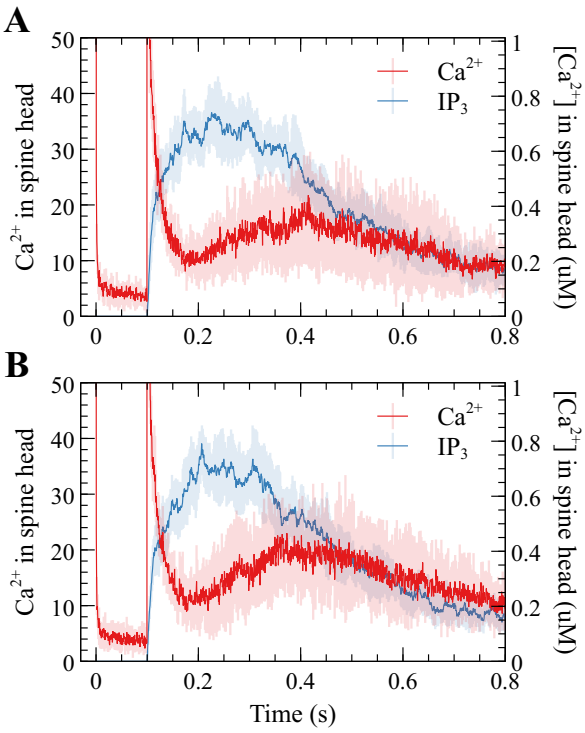

Figure S12: **(A, B)** Averages and standard deviations of 12 Ca^{2+} and IP_3 transients for a single PF stimulus with CF coactivation. Parameter sets B and C from Fig. 6 were used in (A) and (B), respectively. 380 caged IP_3 were used, resulting in a IP_3 transient with a peak value of approximately 1/5th of the peak used for the PF burst stimulus, see e.g. red plot in Fig. 9A. The resulting Ca^{2+} transients reach peak values of about 20 Ca^{2+} = 0.41 μM, in very good agreement with experimental estimates of 0.4 μM, see Piochon et al. (13).

1.7.5 Ataxia - Increasing IP_3

We vary the amount of IP_3 that is part of the PF stimulus and decrease the IP_3R's binding rate k_{on} of IP_3 from their standard values of $IP_{3,peak}$=4.5μM and k_{on} = 83.3 (μMs)$^{-1}$, resp., and investigate how much we need to increase IP_3 for a given decreased k_{on} to recover the usual values of the Ca^{2+} transients peak for the case of PF burst + CF stimuli.

We find that increasing the amount of IP_3 does increase the peak of the resulting Ca^{2+} transients for slower binding of IP_3, but it requires a lot more IP_3 to increase the peak values as required, Fig. S13. Even for peak values of IP_3 around 13μM we can only recover the Ca^{2+} transient's peak for an IP_3 binding rate of $k_{on} \approx 25$ (μMs)$^{-1}$. This significant increase of required IP_3 might quickly reach the saturation of the PLCβ pathway for intermediate to small values of k_{on}.

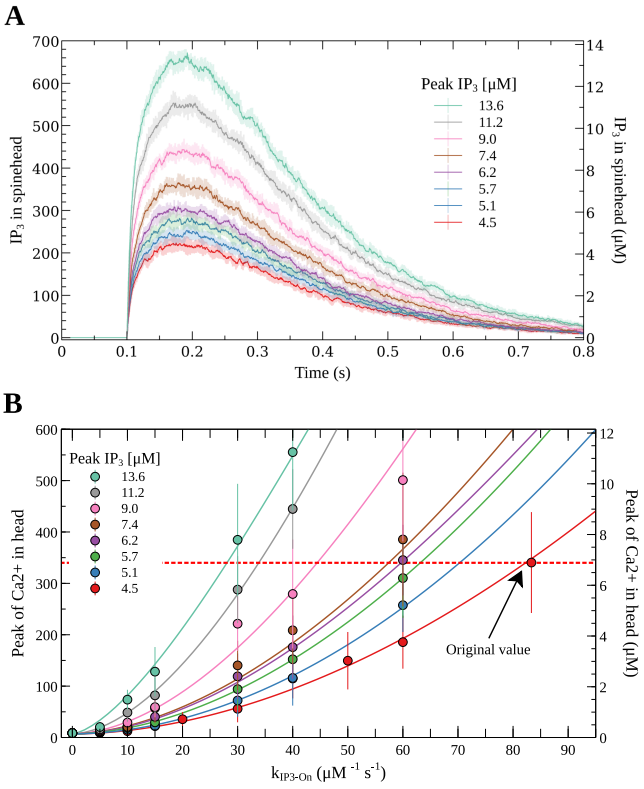

Figure S13: **(A)** Time courses of average [IP_3](t) in the spine head for different amounts of IP_3, **(B)** Values of Ca^{2+} transient peaks against binding rate of IP_3 for different amounts of IP_3. Red dotted line shows Ca^{2+} peak for standard values used in Fig. 7 in the main text.

SUPPORTING REFERENCES

1. Community, B. O., 2019. Blender - a 3D modelling and rendering package. Blender Foundation.

2. Stiles, J. R., D. V. Helden, T. M. B. Jr, E. E. Salpeter,

and M. M. Salpeter, 1996. Miniature endplate current rise times <100 μs from improved dual recordings can be modeled with passive acetylcholine diffusion from a synaptic vesicle. *Proc. Natl. Acad. Sci. USA* 5747–5752.

3. Stiles, J., and T. Bartol, 2001. Monte Carlo methods for simulating realistic synaptic microphysiology using MCell. *Computational Neuroscience: Realistic Modeling for Experimentalists* 87–127.

4. Kerr, R. A., T. M. Bartol, B. Kaminsky, M. Dittrich, J.-C. J. Chang, S. B. Baden, T. J. Sejnowski, and J. R. Stiles, 2008. Fast Monte Carlo Simulation Methods for Biological Reaction-Diffusion Systems in Solution and on Surfaces. *SIAM J Sci Comput* 30:3126.

5. Hoops, S., S. Sahle, R. Gauges, C. Lee, J. Pahle, N. Simus, M. Singhal, L. Xu, P. Mendes, and U. Kummer, 2006. COPASI—a COmplex PAthway SImulator. *Bioinformatics* 22:3067–3074.

6. Franks, K. M., and T. J. Sejnowski, 2002. Complexity of calcium signaling in synaptic spines. *BioEssays* 24:1130–1144.

7. Blackwell, K. T., 2013. Approaches and tools for modeling signaling pathways and calcium dynamics in neurons. *J. Neurosci. Methods* 220:131–140.

8. Moraru, I. I., E. J. Kaftan, B. E. Ehrlich, and J. Watras, 1999. Regulation of type 1 inositol 1,4,5-trisphosphate-gated calcium channels by InsP3 and calcium: Simulation of single channel kinetics based on ligand binding and electrophysiological analysis. *J. Gen. Physiol.* 113:837–49.

9. Doi, T., S. Kuroda, T. Michikawa, and M. Kawato, 2005. Inositol 1,4,5-Trisphosphate-Dependent Ca^{2+} Threshold Dynamics Detect Spike Timing in Cerebellar Purkinje Cells. *J. Neurosci.* 25:950–961.

10. Lee, S. H., B. Schwaller, and E. Neher, 2000. Kinetics of Ca^{2+} binding to parvalbumin in bovine chromaffin cells: implications for [Ca^{2+}] transients of neuronal dendrites. *J. Physiol.* 525 Pt 2:419–432.

11. Schmidt, H., K. M. Stiefel, P. Racay, B. Schwaller, and J. Eilers, 2003. Mutational analysis of dendritic Ca^{2+} kinetics in rodent Purkinje cells: role of parvalbumin and calbindin D28k. *J Physiol* 551:13–32.

12. Antunes, G., A. M. Sebastião, and F. M. Simoes De Souza, 2014. Mechanisms of regulation of olfactory transduction and adaptation in the olfactory cilium. *PLoS ONE* 9.

13. Piochon, C., H. K. Titley, D. H. Simmons, G. Grasselli, Y. Elgersma, and C. Hansel, 2016. Calcium threshold shift enables frequency-independent control of plasticity by an instructive signal. *PNAS* 113:13221–13226.

14. Stauffer, T. P., D. Guerini, and E. Carafoli, 1995. Tissue distribution of the four gene products of the plasma membrane Ca^{2+} pump. A study using specific antibodies. *J. Biol. Chem.* 270:12184–12190.

15. Lytton, J., M. Westlin, S. E. Burk, G. E. Shull, and D. H. MacLennan, 1992. Functional comparisons between isoforms of the sarcoplasmic or endoplasmic reticulum family of calcium pumps. *J. Biol. Chem.* 267:14483–14489.

16. Antunes, G., A. C. Roque, and F. M. Simoes-De-Souza, 2016. Stochastic Induction of Long-Term Potentiation and Long-Term Depression. *Sci. Rep.* 6:30899.

17. Harris, K. M., and J. K. Stevens, 1988. Dendritic spines of rat cerebellar Purkinje cells: serial electron microscopy with reference to their biophysical characteristics. *J. Neurosci.* 8:4455–69.

18. Airaksinen, M. S., J. Eilers, O. Garaschuk, H. Thoenen, A. Konnerth, and M. Meyer, 1997. Ataxia and altered dendritic calcium signaling in mice carrying a targeted null mutation of the calbindin D28k gene. *Proc. Natl. Acad. Sci. U.S.A.* 94:1488–1493.

19. Schmidt, H., and J. Eilers, 2009. Spine neck geometry determines spino-dendritic cross-talk in the presence of mobile endogenous calcium binding proteins. *J Comput Neurosci* 27:229–243.

20. Allbritton, N., T. Meyer, and L. Stryer, 1992. Range of messenger action of calcium ion and inositol 1,4,5-trisphosphate. *Science* 258:1812–1815.

21. Dickinson, G. D., K. L. Ellefsen, S. P. Dawson, J. E. Pearson, and I. Parker, 2016. Hindered cytoplasmic diffusion of inositol trisphosphate restricts its cellular range of action. *Sci. Signal.* 9:ra108–ra108.

22. Kakiuchi, S., S. Yasuda, R. Yamazaki, Y. Teshima, K. Kanda, R. Kakiuchi, and K. Sobue, 1982. Quantitative determinations of calmodulin in the supernatant and particulate fractions of mammalian tissues. *J. Biochem.* 92:1041–1048.

23. Takei, K., T. C. Siidhof, P. Volpe, and P. D. Camilw, 1992. Ca^{2+} Stores in Purkinje Neurons : Endoplasmic Reticulum Subcompartments Demonstrated by the Heterogeneous Distribution of the InsP , Receptor , Ca^{2+} -ATPase , and Calsequestrin. *J. Neurosci.* 12(2):189–505.

24. Wang, S. S., W. Denk, and M. Hausser, 2000. Coincidence detection in single dendritic spines mediated by calcium release. *Nat. Neurosci.* 3:1266–1273.